



CHALMERS
UNIVERSITY OF TECHNOLOGY

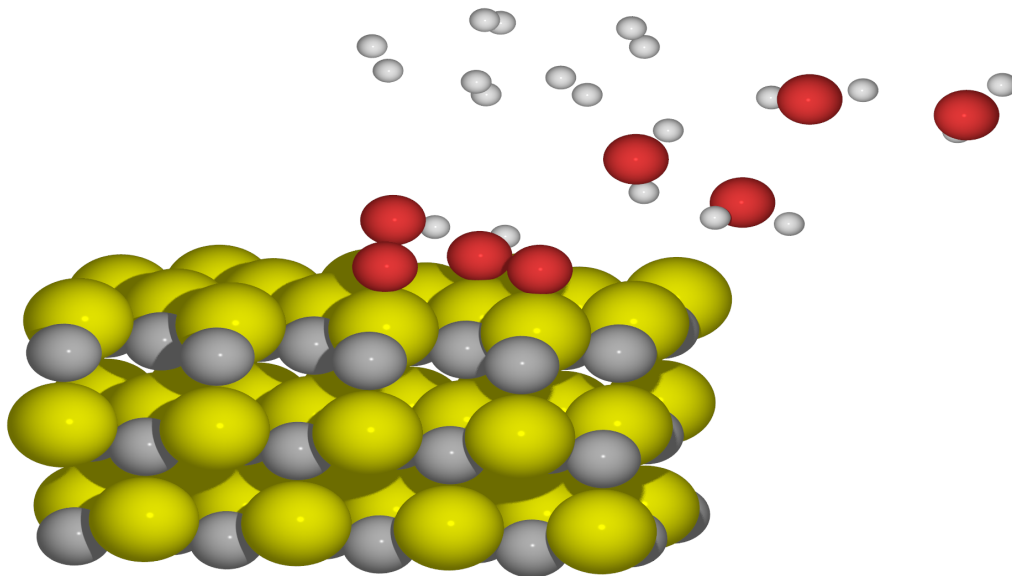


Photo-oxidation of Water on the 3C-SiC Surface: A First-principles Study

Master's thesis in Applied Physics

Fredrik Hansson

MASTER'S THESIS 2016

Photo-oxidation of Water on the 3C-SiC Surface: A First-principles Study

Fredrik Hansson



CHALMERS
UNIVERSITY OF TECHNOLOGY

Department of Physics
Division of Chemical Physics
CHALMERS UNIVERSITY OF TECHNOLOGY
Gothenburg, Sweden 2016

Photo-oxidation of Water on the 3C-SiC Surface: A First-principles Study
FREDRIK HANSSON

© FREDRIK HANSSON, 2016.

Supervisor: Anders Hellman, Department of Physics
Examiner: Anders Hellman, Department of Physics

Master's Thesis 2016
Department of Physics
Division of Chemical Physics
Chalmers University of Technology
SE-412 96 Gothenburg
Telephone +46 31 772 1000

Cover: Adsorbates on a silicon carbide surface with water and hydrogen molecules
in gas phase above the surface.

Typeset in L^AT_EX
Printed by Chalmers Reproservice
Gothenburg, Sweden 2016

Photo-oxidation of Water on the 3C-SiC Surface: A First-principles Study

FREDRIK HANSSON

Department of Physics

Chalmers University of Technology

Abstract

Oxidation of water on the 3C-SiC(111) surface is studied using density functional theory calculations. A four-step oxidation reaction is investigated and a reaction energy landscape is modeled from the free energy of the reaction intermediates. The reaction is studied on the unreconstructed Si surface of the 3C-SiC, which in the (111) cleaving is composed of alternating layers of carbon and silicon atoms. Convergence tests were carried out, first on bulk structure and then on the slab, to obtain a suitable computational model.

The results indicates that the photo-induced water oxidation reaction requires an additional potential of 0.47 V, which, if true would prevent the use of SiC as photoanode for this reaction. The limiting reaction intermediate is the formation of a bare surface site by desorption of HOO*. The calculations suggests that this overpotential is caused by the high surface energy of the bare surface. However, by covering all sites that does not take part in the reaction with hydroxyl groups the overpotential was lowered with about 1 V. As the photoanode is in contact with water, a hydroxyl covered surface is actually a possible structure. Hence, the last result provides a possibility that the overpotential can come down to reasonably values. Future studies should focus on this finding.

Keywords: water-splitting, SiC, photo-oxidation, DFT, hydrogen generation.

Acknowledgements

First and foremost I would like to thank Anders Hellman, for giving me the opportunity to work with this interesting project and for all the help and support! I also want to express my gratitude to all members in the theory group at Chemical Physics, for taking time to answer all my questions and showing interest for my work.

The calculations were performed on resources at Chalmers Centre for Computational Science and Engineering (C3SE) provided by the Swedish National Infrastructure for Computing (SNIC).

Fredrik Hansson, Gothenburg, October 2016

Contents

List of Figures	xi
List of Tables	xiii
1 Introduction	1
1.1 Background	1
1.1.1 Photoelectrochemical water-splitting	2
1.1.2 Previous research	2
1.2 Purpose	4
1.2.1 Research questions	4
1.3 Delimitations	4
2 Theory	5
2.1 Photoelectrochemistry	5
2.1.1 Electrochemical cells and redox reactions	5
2.1.2 Liquid-semiconductor junctions	7
2.1.3 Water-splitting process	9
2.1.4 3C-SiC as a photoanode	10
2.1.5 Overpotential	11
2.2 First-principles calculations	12
2.2.1 The Schrödinger equation	12
2.2.1.1 Ground state from the variational method	13
2.2.1.2 The many-body problem	13
2.2.2 Density functional theory	13
2.2.2.1 The Kohn-Sham ansatz	14
3 Method	17
3.1 Computational setup	17
3.2 Bulk characterization	17
3.2.1 Lattice parameter	18
3.2.2 Bulk modulus	18
3.2.3 Cohesive energy	19
3.2.4 Energy of formation	19
3.3 Surface characterization	19
3.3.1 Surface energy	19
3.3.2 Artificial electric field	20
3.3.3 Bader analysis	20

3.4	Density of states	21
3.5	Reaction pathway and Free energy	22
3.5.1	Free energy calculation	23
3.5.1.1	Entropy and zero-point energy	24
3.5.1.2	Energy landscape and overpotential	26
4	Results	27
4.1	Bulk properties	27
4.1.1	Verifying convergence	27
4.1.2	Bulk characterization	29
4.2	Surface properties	29
4.2.1	Dipole corrections	29
4.2.2	Surface energies	30
4.2.3	Bader analysis	32
4.3	Reaction energy landscape	33
4.4	Electronic configuration	35
4.4.1	Bulk	35
4.4.2	Slab	36
5	Conclusion	39
	Bibliography	41
A	Appendix	I
A.1	Full free energy expressions	II
A.2	Lattice parameter	III
A.3	Dipole correction with hydrogen passivation	IV
A.4	Electronic structure	V
A.5	Free energies	VI

List of Figures

1.1	Number of related citations.	3
2.1	Schematic electrochemical cell.	6
2.2	Band diagram of semiconductor/liquid junction	8
2.3	Band diagram, effect of illumination.	9
2.4	Atomic structure of 3C-SiC(111) slab.	10
2.5	Band diagram, water-splitting and 3C-SiC.	11
3.1	Slab unit used in modeling.	18
3.2	Charge distribution Bader regions.	21
3.3	Schematic energy landscape.	26
4.1	Bulk convergence of energy cutoff and k -point sampling.	28
4.2	Dipole corrections.	30
4.3	Surface energies.	31
4.4	Convergence of vacuum width with respect to adsorption energy.	32
4.5	Energy landscape without hydrogen passivation.	34
4.6	Energy landscape with hydrogen passivation.	35
4.7	Band structure and DOS for bulk 3C-SiC.	36
4.8	DOS for slab without hydrogen passivation.	37
4.9	DOS for slab with hydrogen passivation.	37
A.1	Calculation of the lattice parameter.	III
A.2	Dipole correction with hydrogen passivated slabs.	IV
A.3	DOS, around band gap, without hydrogen passivation.	V
A.4	DOS, around band gap, with hydrogen passivation.	V
A.5	Wavefunctions in the slab.	VI

List of Tables

4.1	Bulk properties.	29
4.2	Bader charge analysis.	32
4.3	Entropies and zero-point energy.	33
A.1	Free energies, 1/2 ML without hydrogen passivation.	VI
A.2	Free energies, 1 ML without hydrogen passivation.	VII
A.3	Free energies, 1/2 ML with hydrogen passivation.	VII

1

Introduction

Several next-generation techniques for renewable energy production are currently being researched, among which photo-induced splitting of water into hydrogen and oxygen molecules is one that has spawned great interest. This technology could potentially allow for hydrogen production with only water and sunlight as resources. Hydrogen can be used to produce higher-value chemical energy and as an energy-vector, which could be important, for example in fuel-cell applications. This project is a theoretical study of the performance of silicon carbide (SiC) in photoelectrochemical applications based on density functional theory (DFT) calculations. In particular, reaction pathways of water-splitting on the SiC surface will be studied based on thermodynamical considerations.

This chapter will give a general introduction to the topic of photoelectrochemical water-splitting and where the research is today. This is followed by a description of the projects scope and purpose as well as what key questions are supposed to be answered upon completion of the project.

1.1 Background

The member countries of the United Nations agreed in late 2015 on keeping the average global temperature increase limited to 1.5–2 °C compared to pre-industrial levels, as described in Article 2 in the Paris Agreement [1]. Moreover, the Intergovernmental Panel on Climate Change (IPCC) stated in their Fifth Assessment Report (AR5) released in 2014 that keeping the temperature increase below 2 °C requires emission levels of greenhouse gases to be reduced by 40-70 percent by 2050 and to nearly zero by 2100 [2]. This implies that innovation and novel ways of producing energy is needed in order to replace the burning of fossil fuel.

Furthermore, the energy consumption is expected to double in the next 50 years [3]. Earth however receives the same amount of energy from the sun in one hour that is consumed globally in one year [4], making conversion of solar energy into useful energy essential in order to meet the climate challenge. A lot of attention has been invested into generating hydrogen by splitting water in photoelectrochemical cells (PEC). There are several configurations of PECs with different electrode types and working mechanisms. The configuration studied in this project consists of a semiconducting anode, where water is decomposed into oxygen molecules and protons. The protons then react into hydrogen molecules at the cathode surface, which for the purpose of this project can be made of any suitable material since the focus of the study will be on the anode reaction. The semiconducting nature of the anode

allows it to absorb photons, which can assist the decomposition of water on the surface. However, the bottleneck in these PECs is currently the photoanode since an appropriate material have not yet been found that satisfies all the requirements needed for it to work [5].

1.1.1 Photoelectrochemical water-splitting

Several materials have been examined as photoanodes since Fujishima and Honda first demonstrated water-splitting through photoelectrolysis in 1972 with a TiO_2 photoanode [6]. In order to work as photoelectrodes materials need to satisfy three requirements, (i) they must be semiconducting with a band gap larger than the redox potential of water at 1.23 eV, (ii) the material needs to be stable against corrosion in the aqueous solution and (iii) the band edges must ideally straddle the redox potential of water [7,8]. In reality the band gap needs to be significantly larger than 1.23 eV due to energy barriers and losses between intermediate reaction steps in the overall water-splitting reaction. This additional energy is an important concept in electrochemistry known as the overpotential and leads to a required total band gap of 1.6–2.4 eV [9]. However, the semiconductor must be able to absorb light in the solar spectra in order to be viable in a self-sustained PEC, which imposes an upper limit of the band gap.

Many of the semiconductors studied so far have been metal oxides thanks to their stability against corrosion [9]. Metal oxides, however, usually have large band gaps leading to a lowered efficiency in the solar spectrum [7]. On the contrary, non-metal oxide semiconductors commonly demonstrate high efficiency but poor stability [7]. Therefore new materials have to be studied in order to develop photoelectrochemical water-splitting as a feasible hydrogen generation technology. A non-metal oxide semiconductor that have received attention is SiC, which exists in more than 170 different polytypes with varying properties. While there are several hexagonal and rhombohedral polytypes there are only one cubic structure, denoted 3C-SiC. The cubic structure is particularly interesting for photoelectrochemical applications since it has an experimental band gap of about 2.4 eV, allowing it to absorb solar light with wavelengths as long as ~ 530 nm, which covers about 40% of the photons in the solar spectrum [10]. Further properties of SiC that makes it interesting in photoelectrochemistry are described in more detail in section 2.1.4.

1.1.2 Previous research

There has been a growing interest in photo-induced water-splitting with SiC in recent years, which is evident from the number of citations in Figure 1.1. Many experimental studies have focused on p-doped SiC since it has been shown to be more durable towards oxidation compared to n-type SiC [8,9]. However, due to the band bending in p-type SiC, excited electrons are transported to the electrode surface and injected into the electrolyte where water or protons are reduced to hydrogen which corresponds to a cathodic reaction. In order to oxidize water into oxygen and protons holes need to be injected from the electrode into the solution, which requires an n-type electrode.

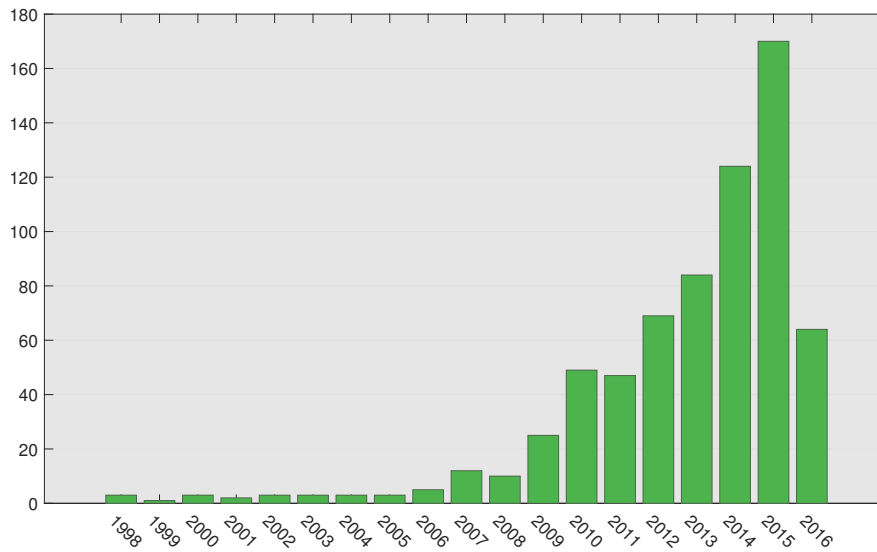


Figure 1.1: Number of citations to publications related to photo-induced water-splitting with SiC. [11]

In 2012, Yasuda et al. showed that both n-type and p-type SiC seem to have band edge potentials capable to split water [8]. They also reported the first self-driven water-splitting cell with SiC photoelectrodes. A constant photocurrent were measured with the p-type sample while the n-type photocurrent decreased with time due to surface oxidation. Thus, they only obtained a working water-splitting cell with a p-type SiC performing a cathodic reaction and have based their subsequent work on investigating this system [7,12].

The oxidation of SiC electrodes acting as photoanodes were further shown by Ma et al. in 2012 by XPS characterizations [13]. PEC experiments in this study were performed only on p-type SiC which generated a cathodic photocurrent under negative bias and a small anodic photocurrent under positive bias. The XPS analysis revealed that the anodic current caused the electrode surface to oxidize.

First-principles calculations by Cicero et al. on the polar 3C-SiC(001) surface have indicated that water dissociation occurs spontaneously on the Si-terminated surface but is an energetically uphill process on the C-terminated surface [14,15]. Furthermore, their calculations suggested that high coverage of hydroxyl groups are favoured to form on the surface. Spontaneous dissociation of water at room temperature on the Si-terminated surface is also consistent with infrared absorption spectroscopy measurements on the (3×2) reconstructed 3C-SiC(100) surface by Amy et al. [16,17].

The work done by Du et al. in 2014 is, to the best of my knowledge, the only first-principles study that investigates the adsorption behaviour and reaction mechanism of water-splitting on 3C-SiC [18]. They studied a reaction pathway in which the water molecule adsorbed dissociatively into H and OH bonded to adjacent Si-atoms. The H atoms then desorbed associatively, leaving the oxygen atom still adsorbed on the surface. Moreover, they studied different surfaces and found that the activation energy for decomposing a water molecule is lowest on the (111) surface.

1.2 Purpose

The study will provide theoretical insights as to the photoelectrochemical performance of 3C-SiC(111) in the water-splitting process. More specifically, its ability to oxidize water molecules as a photoanode is investigated by means of first-principles calculations. The thermodynamics of a four-step reaction path commonly studied for metal oxide photoanodes is tested, which to my knowledge, have not been done previously for a non-metal oxide semiconductor. The research is motivated by the requirement of finding sustainable energy-vectors that can satisfy the future demand in energy.

1.2.1 Research questions

1. Is the reaction path described in reaction R4-R7 (see section 3.5) allowed from thermodynamical considerations?
2. What potential is needed to drive this reaction?

1.3 Delimitations

To completely describe the reaction mechanism both thermodynamics and kinetics must be considered. However, in this project only the thermodynamics will be studied since the energy barriers are difficult to model and therefore beyond the scope of this study.

As the pH is varied the surface would in reality be protonized below the isoelectric point and covered with OH^- above it but this will not be taken into account in this study. The SiC band edge will change with varying pH according to the Nernst equation

$$\Delta E = \frac{k_B T}{e} \ln(10) \times \text{pH} \approx 0.059 \times \text{pH}.$$

However, the redox potential of the water also varies with pH so the effect of excluding this dependence is expected to be small, which have also been demonstrated earlier [9].

All calculations will be performed on intrinsic SiC even though dopants clearly affects the electrochemical properties of the material. The calculations will, however, require very large unit cells in order to obtain dopant species dispersed to normal concentrations.

Cubic SiC is known to have several surface reconstructions which are all important for a conclusive understanding of its photoelectrochemical suitability. The most important surface reconstructions are the (3×3) and $(\sqrt{3} \times \sqrt{3})$ phases apart from the bulk configuration (1×1) [19–21], but only the later one is considered in this project.

2

Theory

Two main concepts of the project is explained in this chapter. Section 2.1 gives an introduction to the photoelectrochemistry and the application of 3C-SiC as a photoanode. This section gives a theoretical framework of PECs as well as the water-splitting reaction studied in this project and is closely related to section 3.5 in the method chapter, where the computational implementation is explained.

Section 2.2 describes the first-principles calculations, namely DFT, used in the project, starting with a theoretical background in quantum mechanics before the numerical method is explained.

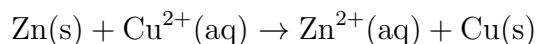
2.1 Photoelectrochemistry

Electrochemistry deals with the interaction of electric potential and chemical reaction. Chemical bonds involve sharing or transfer of electrons between atoms, meaning that electric potential can, in some instances, control chemical reactions. Furthermore, light contains photon energy which can be used to drive a chemical reaction or generate a current in a semiconductor. Thus, photoelectrochemistry adds the interaction of light to electrochemical systems.

The following sections will begin with introducing the general concepts of electrochemical cells and redox reactions and proceed to describe the processes relevant for this work, such as water-splitting and the use of 3C-SiC as a photoanode material.

2.1.1 Electrochemical cells and redox reactions

Chemical reactions involve rearrangement of electrons between bonds or atoms. One major type of reactions are redox reactions, which occurs when one chemical species lose electrons to another species. An example of a redox reaction is the following



where the zinc atoms lose two electrons to the dissolved copper atoms. The event of a reactant losing an electron is called oxidation and the opposite is called reduction when a reactant gains an electron. In the example reaction copper is reduced since it gains electrons from zinc which is therefore oxidized. In order to describe the transfer of electrons in redox reactions the concept of half-reactions is commonly

used, where the total reaction is divided up in an oxidation reaction and a reduction reaction. The half-reactions for the example reaction would thus be



The working principle of electrochemical cells is to separate the reactants, and thereby the half-reactions, but allow the electrons to travel between them to let the reaction proceed. An electrochemical cell typically consists of two electrodes, joined together by a circuit, and immersed in an electrolyte as illustrated in Figure 2.1. The half-reactions will then occur at each of the electrodes. The electrode at which the reduction reaction takes place is called cathode and the electrode where the oxidation reaction takes place is called anode.

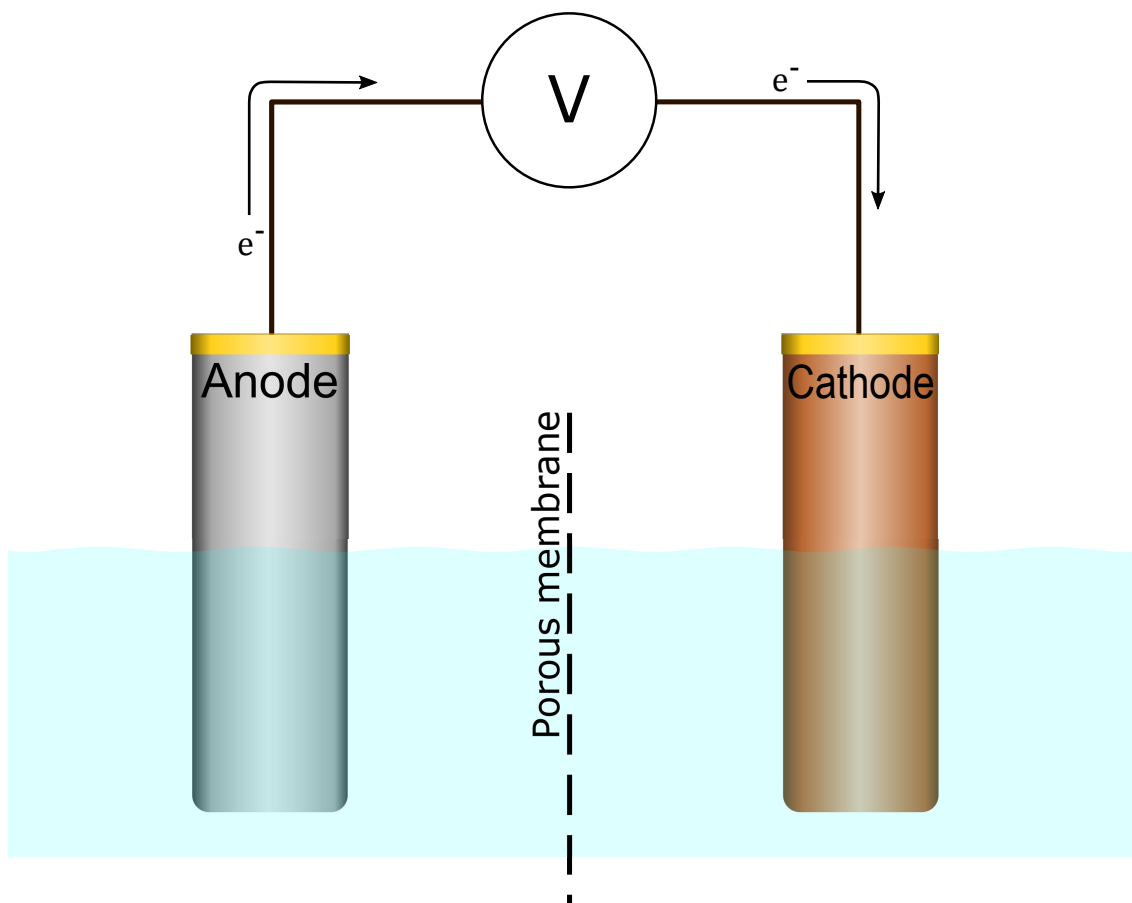
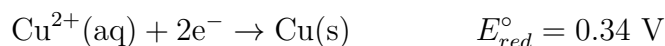


Figure 2.1: Schematic visualization of an electrochemical cell. Electrons travel from the anode to the cathode through the circuit owing to the electric potential. The electrodes are submerged in an electrolyte and separated by a membrane that allows ions to travel through it.

The electrons are transferred between the reactants through the circuit connected to the electrodes and are thus generating an electric current. This implies that

there is a potential difference between the electrodes influencing the electrons to move. This is called the cell potential and is the result of charge transfer across the interface between electrode and electrolyte. The electric potential is a measure of energy per unit charge generated in the redox reaction and can be utilized by coupling electronic devices to the circuit, which is the working principle of batteries and the cell potential corresponds to the voltage of batteries. In fact Alessandro Volta, who is considered to be the inventor of the electrical battery, used zinc and copper discs to generate a current in an electrochemical cell based on the example reaction above [22].

To make it easier to study redox reactions the concept of standard potentials E° is used, which is the individual potential for various half-reactions at standard conditions. The half-reactions above for example have the following standard potentials [22]

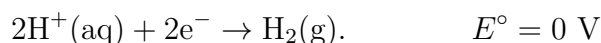


where the subscript refers to the oxidation and reduction potential, respectively. A positive standard potential implies that the half-reaction is favourable. The oxidation potential for a half-reaction is the same as the reduction potential but with opposite sign. The reduction potential of $\text{Zn}^{2+}(\text{aq})$ ions would thus be -0.76 V , indicating that the reduction is not favourable. Tabulated values are commonly stated in reduction potentials.

The cell potential for the redox system above can be determined with the standard potentials accordingly

$$E_{cell}^\circ = E_{ox}^\circ + E_{red}^\circ = 0.76 + 0.34 = 1.10 \text{ V}.$$

An electrochemical cell based on this redox system would thus produce a voltage of 1.10 V. Even though it is easy to determine the cell potential by measurement the standard potentials are much more difficult to determine. It is therefore usually stated relative to a reference potential. A common reference is the hydrogen electrode known as the standard hydrogen electrode (SHE), which means that the standard potential for the hydrogen reduction half-reaction is set to zero by definition [22],



The standard potentials for the half-reactions above are both relative to the SHE.

2.1.2 Liquid-semiconductor junctions

The subject of photoelectrochemistry is highly interdisciplinary, involving chemistry, electrochemistry but also solid state physics and in particular semiconductor physics.

Here the reader will be assumed to have a basic understanding of semiconductor physics, which is otherwise well described in the literature and most notably in the book *Physics of Semiconductor Devices* by Sze [23], considered as being a classic in the field. A more comprehensive description of semiconductor-liquid junctions than that given here is also provided in publications by for example Memming [24, 25].

When a semiconductor is brought in contact with an electrolyte an equilibration of the Fermi energy E_F in the solid and the redox potential eU_{redox} in the electrolyte will take place. When the Fermi energy is above the redox potential an electric current will flow from the semiconductor to the electrolyte until the Fermi energy equals the redox potential. This will give rise to a charge difference between the surface and bulk and thus an internal electric field in the electrode. Figure 2.2 shows the semiconductor/electrolyte system before (left) and after (right) equilibration including the band bending in the semiconductor owing to the charge difference between the bulk and surface. The Fermi energy in the semiconductor is lowered as a consequence of charge transfer to the electrolyte but the difference between the bands and the Fermi energy remains the same in the bulk, which results in the band bending. It is possible to relate the energy scale of the semiconductors Fermi energy to the redox potential through the vacuum level of the reference electrode SHE. The average value of the SHE energy compared to its vacuum is around -4.5 eV [25].

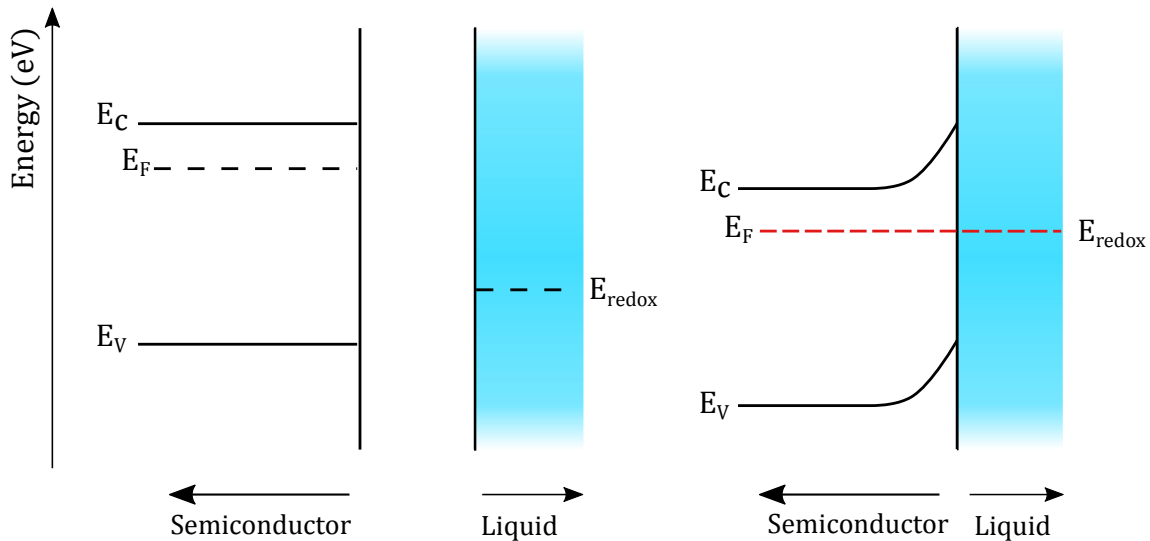


Figure 2.2: The left panel shows the energy levels before the semiconductor and electrolyte is brought together. The right panel shows the band bending after contact. The red dashed line in the right panel represents the equilibrated Fermi energy for the cell. E_C , E_F , E_V and E_{redox} are the conduction band, Fermi energy, valence band and redox potential respectively.

Typically the anode is an n-type semiconductor since the band bending is feasible for the oxidation reaction in the electrolyte. Figure 2.3 shows an electrochemical cell with an n-type semiconductor anode and a metal cathode together with a redox system in the electrolyte. As electron-hole pairs are generated in the depletion

region the electric field generated by the charge difference will result in a flow of holes to the surface where they can recombine with the electrons generated in the oxidation half-reaction. Similarly, the electrons will travel into the bulk and further on through the circuit to the cathode where they will participate in the reduction half-reaction. As a rule of thumb electrons will diffuse "downhill" in the conduction band while holes will diffuse "uphill" in the valence band.

The right panel of Figure 2.3 shows the electrochemical cell under illumination with energy $E_{ph} = h\nu$. This will displace the system from equilibrium by shifting the semiconductors bands and Fermi energy to higher energies. It will also generate electron-hole pairs in the depletion region, which will travel to the electrode surfaces and recombine with the redox couples.

In order for the electrons in the oxidation reaction to be able to recombine with the holes in the anode the valence band must be below the oxidation potential. Similarly the conduction band must be above the reduction potential. Note that the Fermi energy is below the reduction potential before illumination but is increased above the reduction potential as the cell is illuminated, thus allowing the photo-generated electrons in the cathode to reduce the species in the electrolyte [25].

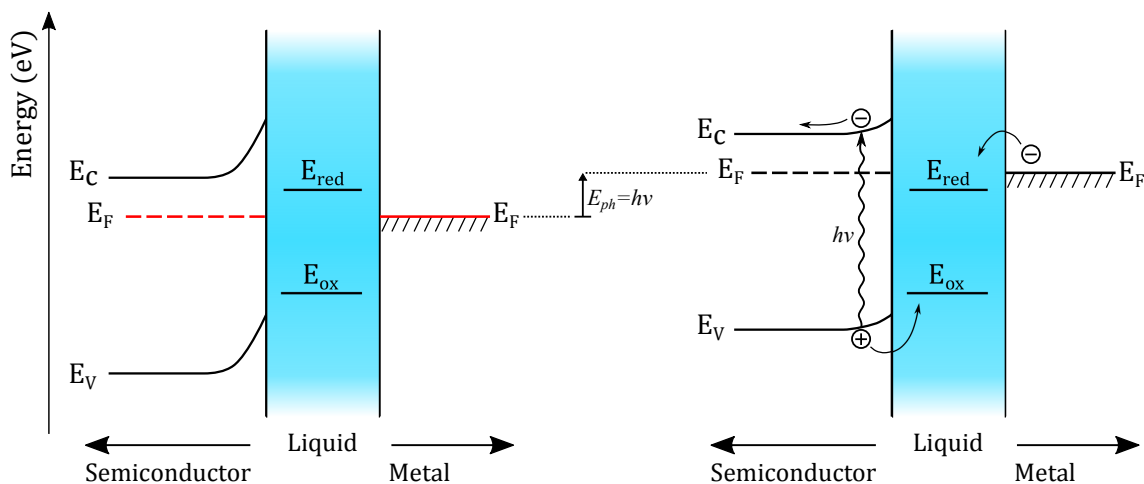
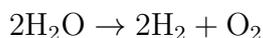


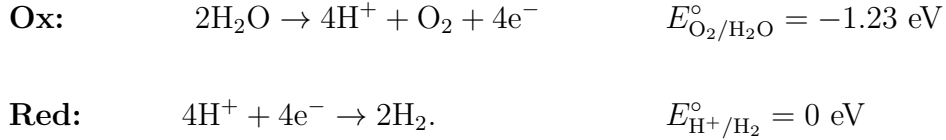
Figure 2.3: The effect of illuminating the photoanode with energy $h\nu$. The left panel shows cell in dark condition and the right panel show the cell under illumination with the photogenerated electron-hole pair included.

2.1.3 Water-splitting process

It is fairly straight forward to consider the redox reaction of water-splitting with the theory above. The overall reaction is



and the half-reactions with corresponding standard potentials are [22]



The reduction potential is zero by definition owing to the standard hydrogen electrode. Note also that the standard potential for the oxidation reaction is negative since oxidizing water molecules is an energetically unfavoured process. It is also clear from the oxidation potential that the semiconductor anode is required to have a band gap larger than 1.23 eV. The reaction starts with the oxidation of water molecules at the anode surface where the photo-generated holes are injected into the water to recombine with the electrons. The molecular oxygen then bubbles off and the protons travel to the cathode where they are reduced to molecular hydrogen by the photo-generated electrons. The oxidation reaction of water and reduction of hydrogen above is commonly known as oxygen evolution reaction (OER) and hydrogen evolution reaction (HER).

2.1.4 3C-SiC as a photoanode

There are more than 170 different polytypes of SiC [17]. The different structures have the notation NX-SiC, where N refer to the layer periodicity and X is the structure (H for hexagonal, R for rhombohedral or C for cubic). The 3C-SiC, which is also known as β -SiC and the only cubic structure that exists, has a zincblende structure i.e. the same atomic structure as diamond but with alternating Si and C atoms. More specifically, the investigated surface is the (111)-surface shown in Figure 2.4. The three-fold periodicity is visible in the side view where the red dashed lines indicate the periodic layers. An important note is that the surface in the figure is in its bulk configuration and have not undergone any surface reconstruction. The surface is, however known to reconstruct in the (3×3) and $(\sqrt{3} \times \sqrt{3})$ phases under different conditions [19–21] but as mentioned in section 1.3, these are not considered in this study.

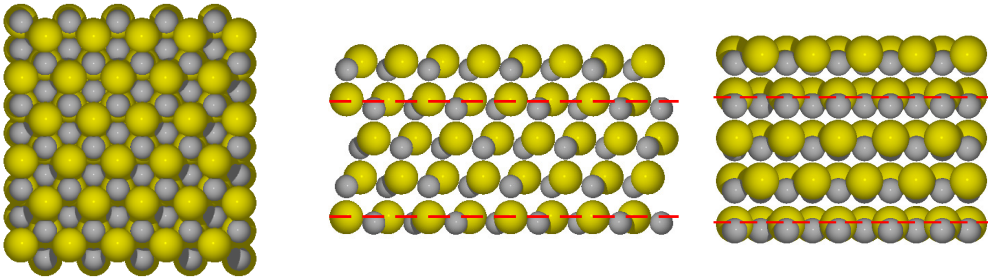


Figure 2.4: A 3C-SiC(111) slab from top and side view. The dashed red lines in the side views highlights the three fold periodicity. Yellow large atoms represent Si atoms and grey small atoms are C atoms.

What makes 3C-SiC interesting in photoanode applications is primarily its band structure. It has a band gap of ~ 2.4 eV [10] and band edges straddling the redox potentials of water. The band gap is thus large enough to cover both the redox potential of 1.23 eV and the overpotential but still small enough to absorb a significant part of the sunlight. The band gap allows 3C-SiC to absorb wavelengths as long as ~ 530 nm, which corresponds to about 40 % of the photons in the solar spectrum [10]. Furthermore, it is also non-toxic and known to be stable [10], which potentially could eliminate the issue of corrosion of the anode.

The photoelectrochemical system with a 3C-SiC anode and the water redox system is presented in Figure 2.5. It illustrates a PEC under illumination where water molecules are oxidized at the 3C-SiC surface by the photo-generated holes. The protons generated in the oxidation reaction then travel to the counter-electrode, a metal in this case, where they are reduced into hydrogen molecules by the photo-generated electrons. Note that the Fermi energies of the electrodes are indeed above the reduction potential and the conduction band below the oxidation potential, according to the requirements described in the end of section 2.1.2. The energies highlighted on the vertical axis are the valence band edge, oxidation potential, reduction potential and conduction band edge relative to the SHE [26].

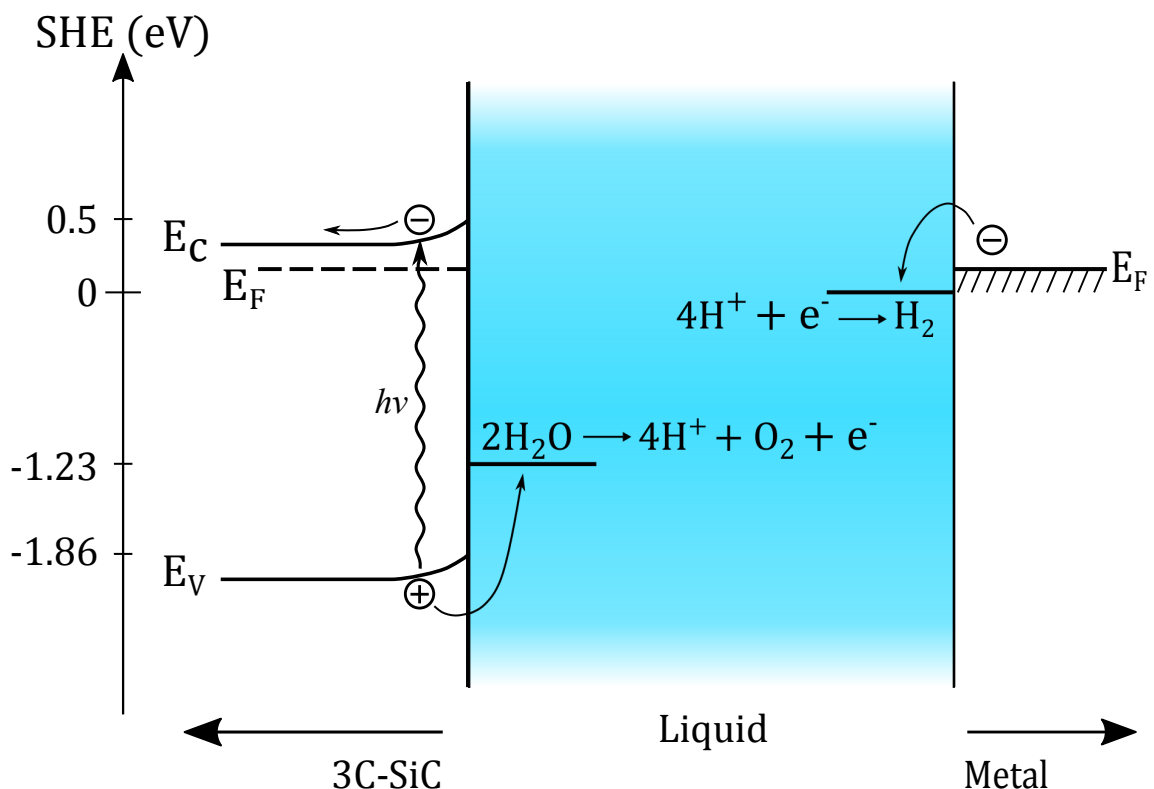


Figure 2.5: Band diagram of an illuminated PEC with a 3C-SiC anode, a metal counter electrode and water in the electrolyte.

2.1.5 Overpotential

A central concept in electrochemistry is the overpotential, which is the extra energy needed to run a process compared to thermodynamic predictions. For an elec-

trochemical cell it can be expressed as the difference between the reversible cell potential and the applied voltage. The overpotential is caused by various reasons, such as electron-hole recombination at the semiconductor surface, its ohmic contact and in the bulk but also activation barriers for intermediate reactions [27].

There can also be a thermodynamic contribution in the event of positive reaction free energies in the energy landscape of the reaction pathway. This should not be confused with the kinetic overpotential which is related to the activation barriers. In order for a reaction to occur all intermediate reaction steps needs to have negative reaction free energies. When positive energies are present the thermodynamic overpotential equals the amount of energy required to remove all uphill steps in the energy landscape [27]. For an electrochemical cell this energy is supplied by controlling the external bias over the cell. The thermodynamic overpotential is important to this project and is further discussed in section 3.5.1.2 below.

2.2 First-principles calculations

The first-principles calculations are carried out using DFT within the semi-local exchange-correlation approximation PBE, described by Perdew, Burke and Ernzerhof [28] in 1996. In order to understand the concepts of DFT, a brief description of relevant topics in quantum mechanics, and in particular the Schrödinger equation is given first. This provides the foundation needed to understand the theory and formalism behind electronic structure modeling with DFT. Furthermore, the theoretical framework of DFT, put forth by Hohenberg, Kohn and Sham, is described.

2.2.1 The Schrödinger equation

Electrons moving in a potential generated by nuclei are described in quantum mechanics by the Schrödinger equation. This is an eigenvalue equation with an Hamiltonian operator \hat{H} acting on the wave functions of the electrons ψ and the eigenvalues being the energy of the system E ,

$$\hat{H}\psi = E\psi. \quad (2.1)$$

The full Hamiltonian for a many-particle system of N electrons and K nuclei is given by the following expression, where \mathbf{r}_i and \mathbf{R}_n are the coordinates of electron i and nucleus n

$$\begin{aligned} \hat{H} = & \sum_{i=1}^N \frac{\hat{p}_i^2}{2m_e} + \sum_{n=1}^K \frac{\hat{P}_n^2}{2M_n} + \frac{1}{4\pi\epsilon_0} \frac{1}{2} \sum_{i,j=1; i \neq j}^N \frac{e^2}{|\mathbf{r}_i - \mathbf{r}_j|} + \\ & - \frac{1}{4\pi\epsilon_0} \sum_{i=1}^N \sum_{n=1}^K \frac{Z_n e^2}{|\mathbf{r}_i - \mathbf{R}_n|} + \frac{1}{4\pi\epsilon_0} \frac{1}{2} \sum_{n,n'=1; n \neq n'}^K \frac{Z_n Z_{n'} e^2}{|\mathbf{R}_n - \mathbf{R}_{n'}|}. \end{aligned} \quad (2.2)$$

Here, upper case letter represents nuclei and lower case represents electrons. The first two terms represents the kinetic energy of electrons and nuclei, respectively, while the last three terms are the coulomb repulsion between electrons, coulomb

attraction between electrons and nuclei and coulomb repulsion between nuclei. This expression is simplified by adopting Hartree atomic units $e = m_e = \hbar = 4\pi\epsilon_0 = 1$. Moreover, the mass of protons and neutrons are about 1836 times larger than the mass of electrons. The nuclei will therefore move much slower than the electrons and can be approximated as being fixed compared to the moving electrons. This approximation, known as the Born-Oppenheimer or adiabatic approximation [29], further simplifies the Hamiltonian in eq 2.2 into

$$\hat{H} = -\frac{1}{2} \sum_{i=1}^N \nabla_i^2 + \frac{1}{2} \sum_{i,j=1;i \neq j}^N \frac{1}{|\mathbf{r}_i - \mathbf{r}_j|} - \sum_{i=1}^N \sum_{n=1}^K \frac{Z_n}{|\mathbf{r}_i - \mathbf{R}_n|}. \quad (2.3)$$

Here, atomic units have been adopted as well as the explicit momentum operator $\hat{p} = -i\hbar\nabla$. This Hamiltonian describes an electronic system where the electrons move in a field generated by the nuclei.

2.2.1.1 Ground state from the variational method

The ground state of a system is given by the wavefunction that yields the lowest energy in eq 2.1. The expectation value of the energy is given by

$$E = \frac{\langle \Psi | \hat{H} | \Psi \rangle}{\langle \Psi | \Psi \rangle} \quad (2.4)$$

where the denominator is a normalization factor. In practice, the ground state is approximated by varying the wavefunction until the energy have converged to a minimum value with some convergence criteria.

2.2.1.2 The many-body problem

The wavefunction is a function of all N electrons, $\Psi = \Psi(\mathbf{r}_1, \dots, \mathbf{r}_N)$, in three spatial dimensions giving $3N$ degrees of freedom. The system described so far by the Schrödinger equation and with this wavefunction is a many-electron system with N electrons interacting with each other simultaneously. This render all problems, larger than the most simple ones, to difficult to be solved numerically.

Electrons are fermions and must therefore obey the Pauli exclusion principle, which states that two fermions can not occupy the same quantum state. The many-electron wavefunction is described as anti-symmetric, meaning that it changes sign if two electrons quantum states are exchanged

$$\Psi(\mathbf{r}_1, \dots, \mathbf{r}_i, \dots, \mathbf{r}_j, \dots, \mathbf{r}_N) = -\Psi(\mathbf{r}_1, \dots, \mathbf{r}_j, \dots, \mathbf{r}_i, \dots, \mathbf{r}_N). \quad (2.5)$$

Furthermore, the second term in eq 2.3 results in all electrons being correlated in their movements. These exchange and correlation effects are important concepts in numerical approaches to approximate the Schrödinger equation.

2.2.2 Density functional theory

The two most important methods to approximate the Schrödinger equation to this day have been the Hartree-Fock method, where the many-electron wavefunction is

approximated as N one-electron wavefunctions, and DFT, where the electron density is treated instead of the many-body wavefunction when solving the Schrödinger equation. For solids and larger systems in condensed matter physics the most common approach is DFT. The method originates from two papers published in 1964 by Hohenberg and Kohn [30] and 1965 by Kohn and Sham [31], where the so called Hohenberg-Kohn theorems and Kohn-Sham ansatz are formulated. The theorems states that all properties of a system and its ground state can be described by the particle density of the system, and the ansatz describes an approach to solve the functional formulation based on the two theorems. The Hohenberg-Kohn theorems are stated below as formulated by Martin [32].

In electronic structure calculations within DFT the electrons are assumed to move in an external potential, V_{ext} , generated by the fixed nuclei. This corresponds to the last term in the electronic Hamiltonian in eq 2.3 with the electron-nuclei coulomb interaction expressed as an external potential.

H-K theorem 1: For any system of interacting particles in an external potential $V_{ext}(\mathbf{r})$, the potential $V_{ext}(\mathbf{r})$ is determined uniquely, except for a constant, by the ground state particle density $n_0(\mathbf{r})$.

H-K theorem 2: A universal functional for the energy $E[n]$ in terms of the density $n(\mathbf{r})$ can be defined, valid for any external potential $V_{ext}(\mathbf{r})$. For any particular $V_{ext}(\mathbf{r})$, the exact ground state energy of the system is the global minimum value of this functional, and the density $n(\mathbf{r})$ that minimizes the functional is the exact ground state density $n_0(\mathbf{r})$.

The achievement of these theorems is the proof of existence of a functional, given by the ground state particle density, that describes all the properties of the system. However, the theorems only proves the existence of these functionals but not the their form. The Kohn-Sham ansatz, described a year later, provided a framework for approximating these functionals thus giving practical meaning to DFT.

2.2.2.1 The Kohn-Sham ansatz

The Hohenberg-Kohn theorems above is a formulation of DFT for many-body interacting systems and is therefore still to complex for practical applications. The idea behind the Kohn-Sham ansatz is to instead provide a non-interacting particle description of the problem based on the Hohenberg-Kohn theorems by assuming that the ground state density of the many-body interacting system equals a fictitious non-interacting system ground state density. This new system is described by the Kohn-Sham adaption of the Schrödinger equation in eq 2.6, where the kinetic term is the same as above but the non-interacting particles are assumed to move around in an effective local potential $V_{eff}(\mathbf{r})$

$$H_{KS}^{\sigma} \psi_i^{\sigma} = \varepsilon_i^{\sigma} \psi_i^{\sigma}. \quad (2.6)$$

Here σ and i denotes spin and state respectively, and ψ_i^{σ} are known as Kohn-Sham orbitals with ε_i being the orbital energies. The Hamiltonian has the form

$$H_{KS}^\sigma = -\frac{1}{2}\nabla^2 + V_{eff}^\sigma(\mathbf{r}) \quad (2.7)$$

where the effective potential is given by

$$\begin{aligned} V_{eff}^\sigma(\mathbf{r}) &= V_{ext}(\mathbf{r}) + V_{Hartree}(\mathbf{r}) + V_{xc}^\sigma(\mathbf{r}) = \\ &= V_{ext}(\mathbf{r}) + \frac{\delta E_{Hartree}}{\delta n(\mathbf{r}, \sigma)} + \frac{\delta E_{xc}}{\delta n(\mathbf{r}, \sigma)}. \end{aligned} \quad (2.8)$$

Here V_{ext} is the same external potential as previously, $V_{Hartree}$ is the electron-electron coulomb interaction corresponding to the second term in eq 2.3 and commonly known as the Hartree potential in DFT. The third term V_{xc} is the exchange-correlation potential where all the many-body effects are collected and is the only unknown term in the Kohn-Sham description of the particle system. The equations 2.6-2.8 are known as the Kohn-Sham equations.

The total energy of the system is then given by

$$E = \sum_{\sigma} \sum_{i=1}^N \varepsilon_i^{\sigma} - \frac{1}{2} \int d^3r d^3r' \frac{n(\mathbf{r})n(\mathbf{r}')}{|\mathbf{r} - \mathbf{r}'|} + E_{xc}[n] - \int d^3r V_{xc}[n(\mathbf{r})]n(\mathbf{r}). \quad (2.9)$$

According to the Hohenberg-Kohn theorems this energy is minimized by the ground state density, which also determines the external potential used to find the Kohn-Sham orbital eigenvalues. The density for an N -particle system with spin σ is given by

$$n(\mathbf{r}) = \sum_{\sigma} n(\mathbf{r}, \sigma) = \sum_{\sigma} \sum_{i=1}^N |\psi_i^{\sigma}(\mathbf{r})|^2. \quad (2.10)$$

Note that the Kohn-Sham orbital eigenvalues does not have much physical meaning since they alone do not represent the total energy of the system, in contrast to the Schrödinger equation in eq 2.1.

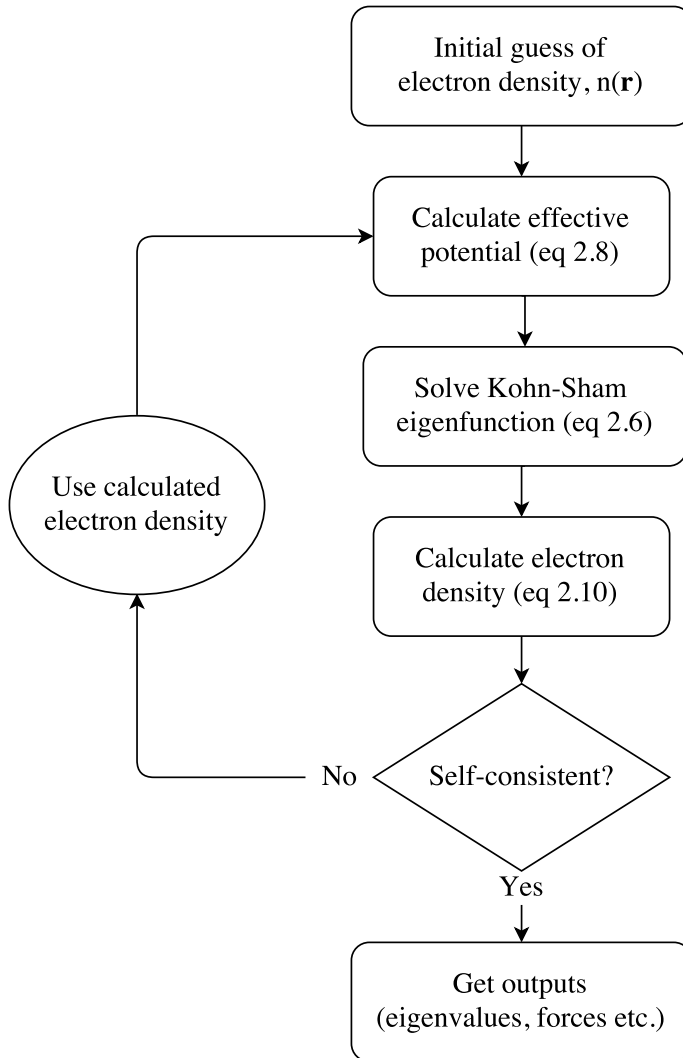
So far no approximations have been made, meaning that eq 2.6-2.8 gives an exact description of the many-body system where all the many-body effects are moved to the exchange-correlation term. However, since $E_{xc}[n]$ is unknown it needs to be approximated in order to solve the Kohn-Sham equations. The first and most simple approximation is the local density approximation (LDA) where only the local particle density in \mathbf{r} is taken into account. Even though LDA have been successful it is rarely used today. Instead different forms of generalized-gradient approximations (GGA) have become standard. These are semi-local approximations since they also include the magnitude of the first density gradient. The general expressions of LDA and GGA is given in the equations below, where ϵ_{xc} denotes the exchange-correlation energy density, and clearly shows their difference

$$E_{xc}^{LDA}[n] = \int d^3r n(\mathbf{r}) \epsilon_{xc}[n] \quad (2.11)$$

$$E_{xc}^{GGA}[n] = \int d^3r n(\mathbf{r}) \epsilon_{xc}[n, |\nabla n|]. \quad (2.12)$$

The PBE functional mentioned in the beginning of section 2.2 belongs to the GGAs and is the most common approximation to the exchange-correlation energy functional used today [33].

Finally, the ground state is found by solving the Kohn-Sham equations 2.6-2.8 self-consistently. The procedure is summarized in the following flow chart.



3

Method

This chapter describes the computational setup along with analysing procedures used. The parameters and computational settings used to model the main results are stated in section 3.1 in order to give the reader a quick understanding of how the calculations are performed. The following sections detail the analysing methods used to converge the parameters summarized in section 3.1 and to investigate the structure.

Finally, in section 3.5 the water-splitting reaction pathway, considered in this study, is presented along with the thermodynamical approach to analyze each intermediate reaction step.

3.1 Computational setup

The calculations are performed with the GPAW software, which is based on the projector-augmented wave method to describe the core wave functions [34]. The atomic structures were constructed in the Atomic Simulation Environment (ASE), which also provides functions to analyze calculations.

The wave functions are expanded with a plane wave basis set using a 600 eV energy cutoff. The exchange-correlation energy is calculated within the generalised gradient approximation (GGA), using the PBE functional [28]. The lattice parameter was found to be 4.39 Å with this functional. The slab thickness consists of eight atomic layers where the atomic species in each layer alternates between Si and C atoms, as shown in the left panel of Figure 3.1. The right panel shows the unit cell in top view. The vacuum width between the slabs, not counting any adsorbates if present, is set to 14 Å and the k -point sampling is made with a $4 \times 4 \times 1$ Monkhorst-Pack mesh [35]. The structure relaxations are carried out with the BFGSLineSearch algorithm with a force convergence criteria of 0.05 eV/Å.

All calculations with molecules and slabs with adsorbates bonded to the surface have been spin-polarized. The magnetic moment was found to be zero in the free slab and calculations involving free slabs and bulk have therefore been spin-paired.

3.2 Bulk characterization

There are two reasons for characterizing the bulk. Converging the lattice parameter, which is used as an input in the calculations, and also verifying that the calculations reproduce known values of material properties. The obtained bulk properties

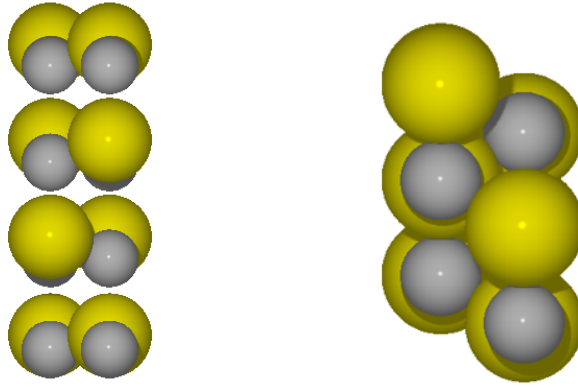


Figure 3.1: The slab used in the main calculations after convergence tests seen from the side (left) and top (right). The yellow larger atoms are Si and the grey smaller atoms are C.

are presented in presented in Table 4.1 and compared to reference values from the literature.

However, not only material properties are computed to converge calculation parameters. The energy cutoff radius as well as k -point sampling distribution are converged with respect to the crystal structure energy obtained by the calculations, with a convergence criteria of 10 meV, and are presented in section 4.1.1.

3.2.1 Lattice parameter

The PBE functional tends to overestimate the lattice parameter [36]. It therefore needs to be determined theoretically since experimental values would induce a strain in the material due to the discrepancy. The lattice parameter is found by varying the cell size around an initial value and the energy is calculated for each variation. If the equilibrium volume is captured in the variation, this will give rise to an energy parabola with the minimum in the equilibrium volume (see Figure A.1 in the appendix). This is straight forward since the energy of the system increases if the crystal is strained, which is what changing the volume implicates, and should therefore have a lowest energy in the equilibrium volume. The curve fitting along the calculated energies at different volumes and the determination of equilibrium volume is done with the EquationOfState class in ASE, from which the theoretical lattice parameter is found.

3.2.2 Bulk modulus

The bulk modulus measure materials resistance towards compression. The bulk modulus of an object is defined as the change in pressure under an infinitesimal change in the objects volume

$$B = -V \frac{dP}{dV}. \quad (3.1)$$

This can, however be rewritten into

$$B = V \frac{d^2 E}{dV^2}. \quad (3.2)$$

This quantity can easily be determined by following the same procedure as for finding the lattice parameter described in section 3.2.1. The `EquationOfState` class in ASE generates an energy-volume curve shaped as a quadratic function, which is used to find the bulk modulus.

3.2.3 Cohesive energy

The cohesive and formation energy of bulk SiC was calculated and compared to literature to further verify that the structure is well described in the calculations.

The cohesive energy is a measure of how well the atoms in a crystal sticks together. It is defined here as the difference in energy between the bulk structure and the isolated Si and C atoms, as in eq 3.3 where E_{SiC} is the energy per SiC-pair in the bulk and E_{Si} and E_C are the energies of isolated Si and C atoms, respectively.

$$E_{coh} = E_{SiC} - (E_{Si} + E_C) \quad (3.3)$$

3.2.4 Energy of formation

The energy of formation is the change in energy when a composite material is formed from its component compounds. Silicon has diamond crystal structure but pure carbon in its solid state exists in several different polytypes. Here the diamond structure of carbon is used to calculate the energy of formation for SiC since the infinite bulk in the calculations does not have any dangling bonds as in graphene or van der Waals forces as in graphite, which are not well described in DFT. The energy of formation is given by eq 3.4, where E_{SiC} is the energy per atom of bulk SiC and E_{Si}^{bulk} and E_C^{bulk} is the energy per atom of pure silicon and carbon crystal, respectively.

$$E_{form} = E_{SiC} - (E_{Si}^{bulk} + E_C^{bulk}) \quad (3.4)$$

3.3 Surface characterization

The main reasons to study the bulk is to verify that the calculations perform properly and to converge calculation parameters but the water-splitting reaction studied in this project occurs on a surface. Parameters must therefore be further converged with respect to the surface and physical properties must be studied in order to understand the interaction between 3C-SiC and adsorbates.

3.3.1 Surface energy

The formation of surfaces are associated with an energy cost due to the cohesion between the atoms, which prefer to stay bonded, and the dangling bonds that occurs

in the surface. The surface energy have been calculated and used to measure the convergence of certain parameters in the calculations, using eq 3.5. Here, E_{slab} is the energy of the slab, E_{bulk} is the energy of bulk SiC per SiC-pair, N is the number of SiC-pairs in the slab and A is the surface area. The expression is divided by two in order to account for both surfaces in the slab.

$$E_{surf} = \frac{E_{slab} - N \cdot E_{bulk}}{2A} \quad (3.5)$$

The surface energy is calculated with different vacuum width, number of k -points, energy cutoff and slab thickness in order to verify the accuracy for the surface calculations.

3.3.2 Artificial electric field

The calculations employ periodic boundary conditions in all directions for the atomic structure and wave functions, and consequently, also the electrostatic potential (ESP) between the surfaces. However, adsorbates or asymmetric slabs, with different dipole densities in the surfaces, could in reality have different ESP on both sides of the slab but the periodicity enforces a gradient in this potential over the vacuum region. Thus, the periodic potential might create a uniform electric field between the slabs that might affect surface reactions. A method to compensate for this field, by introducing a dipole field, was developed first by Neugebauer and Scheffler in 1992 [37] and later improved by Bengtsson in 1998 [38].

The significance of the artificial electric field was investigated with a ten atom layer thick slab with an oxygen atom adsorbed on the Si-terminated surface. GPAW does not support dipole correction with plane-waves so the wavefunctions were expanded using the finite-difference method.

3.3.3 Bader analysis

The distribution of charge in the SiC is studied using a method developed by Richard Bader [39]. He suggested that the atomic boundaries can be defined as regions, known as Bader regions, in real space based on the charge density. The total charge of the atoms is then obtained by integrating the charge density over the Bader regions.

The Bader regions are bounded by so-called zero-flux surfaces. These are found by drawing trajectories along the steepest ascent path of the charge density gradient $\nabla\rho(\mathbf{r})$ in the 3D real space. Thus, $\nabla\rho(\mathbf{r})$ is first calculated in one grid point, then a small step is taken in the path of steepest ascent to a new grid point where $\nabla\rho(\mathbf{r})$ is again calculated and so forth until a maximum is found. This will yield surfaces with no charge density flux normal to the surface, hence zero-flux surface. Figure 3.2 shows the charge density of a CO molecule as an example with the zero-flux surface as the vertical line between the atoms. All trajectories drawn on the right side of the zero-flux surface will end up on the oxygen atom. Similarly, all trajectories drawn on the left side will end up on the carbon atom but no trajectories will cross the zero-flux surface.

An algorithm developed by Henkelman et al. have been used in this project to carry out the Bader charge analysis [40].

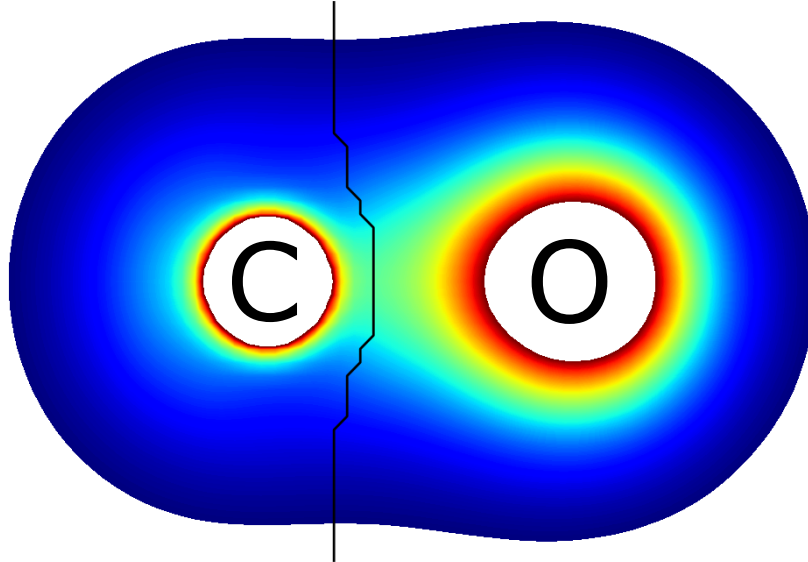


Figure 3.2: Charge density of a CO molecule with the zero-flux surface as the vertical line between the atoms.

3.4 Density of states

The density of states describes the number of states, per unit volume, within the energy interval $[E, E+dE]$ and is obtained by integrating the eigenvalues over the Brillouin zone as in eq 3.6. Here Ω_{BZ} is the volume of the Brillouin zone and $\varepsilon_{i,\mathbf{k}}$ the eigenvalues in the i th band.

$$\rho(\varepsilon) = \sum_i \int_{\Omega_{BZ}} \delta(\varepsilon - \varepsilon_{i,\mathbf{k}}) \frac{d^3\mathbf{k}}{\Omega_{BZ}} \quad (3.6)$$

However, the number of k -points must be finite in numerical implementations so the integral is evaluated as a weighted sum over some "special" k -points,

$$\rho(\varepsilon) \approx \sum_i \sum_{n=1}^{N_{kpt}} w_n \delta(\varepsilon - \varepsilon_{i,\mathbf{k}_n}). \quad (3.7)$$

The delta function is smeared in order to better sample it on a coarse grid. The ASE software uses a gaussian smearing with a smearing width σ , which in this study is set to the default width of $\sigma = 0.1$.

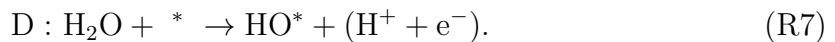
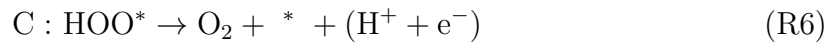
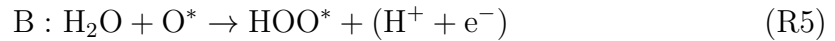
$$\delta(\varepsilon - \varepsilon_{i,\mathbf{k}_n}) \quad \rightarrow \quad f = \frac{1}{\sigma\sqrt{\pi}} \exp \left[- \left(\frac{\varepsilon - \varepsilon_{i,\mathbf{k}_n}}{\sigma} \right)^2 \right] \quad (3.8)$$

3.5 Reaction pathway and Free energy

The overall water-splitting reaction is stated in reaction R1 with the OER and HER in reaction R2-R3,



The focus of this project is to investigate the reaction path in the OER from a thermodynamic perspective on the 3C-SiC(111) surface. Under acidic conditions the OER in R2 is assumed to occur in a sequence of the four elementary reactions in R4-R7, where a * represents a surface vacancy or a species bound to the surface. This reaction path have been studied previously on different semiconductor surfaces [41–45],



Each elementary reaction generates an electron, which travels through the SiC to the cathode, and a proton, which traverse the electrolyte and is reduced by the generated electron at the cathode.

As described in section 1.1.2, previous studies of the interaction between water and the 3C-SiC(111) surface have established that water dissociates spontaneously at room temperature into OH^* and H^* at adjacent Si atoms on the Si-terminated surface. Furthermore, studies have shown that the surface is passivated by hydroxyl groups. Therefore the first step in the reaction pathway is taken to be the hydroxylated surface and no hydrogen saturation is considered. Direct recombination of surface oxygen is also not considered since the activation barrier is expected to be large [41].

Furthermore, the effect of different coverages and hydrogen passivations are studied. Calculations are performed with the dangling bonds on the bottom surface either fully saturated with hydrogen or without saturation. Two different adsorbate coverages are considered, namely full coverage (1 ML) and half coverage (1/2 ML), with adsorbates bonding only to the Si atoms on the surface. The unit cells has

only two available surface sites for adsorbates to bind to. A 1/2 ML coverage thus implies that all adsorbates are reaction precursors. For the 1 ML coverage the free site have been saturated with a hydroxyl group throughout the reaction pathway.

3.5.1 Free energy calculation

Gibbs free energy is defined as

$$G = H - TS \quad (3.9)$$

where H is the enthalpy, T is the temperature and S is the entropy. Furthermore, the enthalpy includes a zero-point energy correction of the ground state, giving the following expression for Gibbs free energy, where ZPE is the zero-point energy correction and E_{DFT} is the total energy obtained in the calculations

$$G = E_{DFT} + ZPE - TS. \quad (3.10)$$

The zero-point energy is a consequence of the uncertainty principle. The potential energy around the ground state can be viewed as a harmonic oscillator. The minimum energy for a classical harmonic oscillator is uniquely determined by the equilibrium position where both position and momentum are known exactly. However, due to Heisenberg's uncertainty principle, the lowest quantum mechanical energy possible is shifted up in energy by $\frac{1}{2}\hbar\omega$, where ω is the angular frequency of the harmonic oscillator.

The free energy of the reaction mechanism described in R4-R7 is determined by the method developed by Nørskov and Rossmeisl in ref. [46] and can be summarized in the following steps.

1. The standard potentials are considered in reference to the standard hydrogen potential. The standard potential of $\text{H}^+(\text{g}) + \text{e}^- \rightarrow 1/2\text{H}_2(\text{g})$ then equals zero by definition. The free energy of $\text{H}^+(\text{aq}) + \text{e}^-$ in the reaction path can then be considered equal to the free energy of $1/2\text{H}_2(\text{g})$ at standard conditions.
2. The enthalpy difference of a reaction, ΔH , is calculated as the DFT energy difference between the reaction products and reactants. The difference in entropy and zero-point energy is obtained from DFT calculations of vibrational frequencies of each reaction species. Vibrational, rotational and translational entropies are considered for molecules and are obtained entirely by calculations. All degrees of freedom for the adsorbates are, however, treated harmonically since they typically do not have any translational or vibrational movement because of the strong chemisorption.
3. The effect of potential bias on each intermediate reaction is included by shifting the free energy by $\Delta G_U = -eU$, where U is the electrode bias relative to the SHE.
4. The modeled electrode is submerged in liquid water so the entropy of water is determined at 0.035 bar since this is the equilibrium pressure at room temperature, meaning that the free energy is the same for molecules in gaseous and liquid phase.

5. The oxygen molecule is not well described in DFT and its energy is therefore determined by considering the experimental value of $\Delta G = 4.92$ eV for the total water-splitting reaction $2\text{H}_2\text{O} \rightarrow \text{O}_2 + 2\text{H}_2$. The total energy of the oxygen molecule is thus obtained through

$$E_{\text{O}_2} = 4.92 + 2G_{\text{H}_2\text{O}} - 2G_{\text{H}_2} - (\text{ZPE} - TS)_{\text{O}_2}. \quad (3.11)$$

After inserting this in eq 3.10 the final Gibbs free energy expression for the oxygen molecule becomes

$$G_{\text{O}_2} = 4.92 + 2G_{\text{H}_2\text{O}} - 2G_{\text{H}_2}. \quad (3.12)$$

This approach have been used and motivated in ref. [41, 42, 46].

Finally, the free energy of each intermediate reaction step in R4-R7 is calculated as

$$\Delta G_A = \Delta E_A + \frac{1}{2}E_{\text{H}_2} + (\Delta\text{ZPE} - T\Delta S)_A - eU \quad (3.13a)$$

$$\Delta G_B = \Delta E_B + \frac{1}{2}E_{\text{H}_2} - E_{\text{H}_2\text{O}} + (\Delta\text{ZPE} - T\Delta S)_B - eU \quad (3.13b)$$

$$\Delta G_C = 4.92 + \Delta E_C + 2E_{\text{H}_2\text{O}} - \frac{3}{2}E_{\text{H}_2} + (\Delta\text{ZPE} - T\Delta S)_C - eU \quad (3.13c)$$

$$\Delta G_D = \Delta E_D + \frac{1}{2}E_{\text{H}_2} - E_{\text{H}_2\text{O}} + (\Delta\text{ZPE} - T\Delta S)_D - eU. \quad (3.13d)$$

Here, all the ΔE_i are the energy difference between the slabs with different adsorbates in reaction i . Note also how the free energy expression for reaction C is different from the others due to the oxygen molecule generated in the reaction. A more thorough and detailed explanation of the O_2 treatment as well as the full expressions of the free energies in eq. 3.13a-3.13d is available in appendix A.1.

3.5.1.1 Entropy and zero-point energy

Entropies and zero-point energies are calculated for the adsorbates (O^* , HO^* and HOO^*) as well as the dissolved O_2 , H^+ and H_2O using the ASE-modules Vibrations and Thermochemistry. The Vibrations module calculates the vibrational modes of the species by treating them as harmonic oscillators. The zero-point energy is then calculated using the vibration frequencies as described above in section 3.5.1. The Thermochemistry module use statistical mechanics to calculate entropy. The dissolved species are assumed to behave as an ideal gas, meaning that translational, rotational and vibrational modes of motion are all included, while the adsorbates are assumed to only have vibrational motion thanks to strong adsorption to the surface. The following text will briefly state the relations used to calculate the entropies without derivations. The theory is thoroughly described in the literature, for instance by Chorkendorff [47] and Cramer [48].

The total entropy can be expressed as the sum of all entropic modes as described in eq 3.14. The first three terms represents the three modes of motion of an ideal gas particle, translation, rotation and vibration which are all expressed in standard pressure, 101325 Pa. The last two terms accounts for electronic excitations and deviation from standard pressure, respectively. The O₂ and H₂ molecules are treated in standard pressure, meaning that the pressure term in eq 3.14 vanishes. However, in order to model the water molecule as a liquid its entropy is calculated in 0.035 bar since water vapor and liquid has the same chemical potential at this pressure $\mu_{\text{H}_2\text{O}}(35 \text{ mbar}, l) = \mu_{\text{H}_2\text{O}}(35 \text{ mbar}, g)$. The temperature is always set to room temperature 298.15 K.

$$S = S_{trans} + S_{rot} + S_{vib} + S_{elec} - k_B \ln \frac{P}{P^\circ} \quad (3.14)$$

The entropic terms are stated in eq 3.15a-3.15e where M is the molecule mass, I moment of inertia, σ symmetry number, df degrees of freedom, ε_i vibration energy and s the spin. Equation 3.15b is used for linear molecules and eq 3.15c for nonlinear molecules.

$$S_{trans} = k_B \left\{ \ln \left[\left(\frac{2\pi M k_B T}{h^2} \right)^{3/2} \frac{k_B T}{P^\circ} \right] + \frac{5}{2} \right\} \quad (3.15a)$$

$$S_{rot}^{linear} = k_B \left[\ln \left(\frac{8\pi^2 I k_B T}{\sigma h^2} \right) + 1 \right] \quad (3.15b)$$

$$S_{rot}^{nonlinear} = k_B \left\{ \ln \left[\frac{\sqrt{\pi I_A I_B I_C}}{\sigma} \left(\frac{8\pi^2 k_B T}{h^2} \right)^{3/2} \right] + \frac{3}{2} \right\} \quad (3.15c)$$

$$S_{vib} = k_B \sum_i^{df} \left[\frac{\varepsilon_i}{k_B T [\exp(\varepsilon_i/k_B T) - 1]} - \ln \left(1 - \exp(-\varepsilon_i/k_B T) \right) \right] \quad (3.15d)$$

$$S_{elec} = k_B \cdot \ln(2s + 1) \quad (3.15e)$$

The adsorbates are assumed to be bonded strong enough to have negligible translational and rotational motion. The entropy is therefore determined by treating all degrees of freedom harmonically in eq 3.16. Here all N atoms are moved in each spatial direction, giving $3N$ degrees of freedom.

$$S_{harm} = k_B \ln \prod_i^{3N} \frac{1}{1 - \exp(-\varepsilon_i/k_B T)} \quad (3.16)$$

3.5.1.2 Energy landscape and overpotential

The energy landscape is visualized by plotting the free energy differences in eq 3.13a-3.13d as shown in figure 3.3. By inspecting the free energy expressions (more comprehensively stated in appendix A.1) it can be seen that their sum cancel out all terms but the experimental value 4.92 eV and the electrode biases. The difference between the final and initial step in the energy landscape should thus equal

$$G_{final} - G_{initial} = 4.92 - 4eU. \quad (3.17)$$

The overpotential can be found in the energy landscape by identifying the largest positive free energy step.

$$\eta = \max(0, \Delta G_A, \Delta G_B, \Delta G_C, \Delta G_D). \quad (3.18)$$

In order for the water-splitting reaction to be self-driven all steps must be negative or zero with applied external bias.

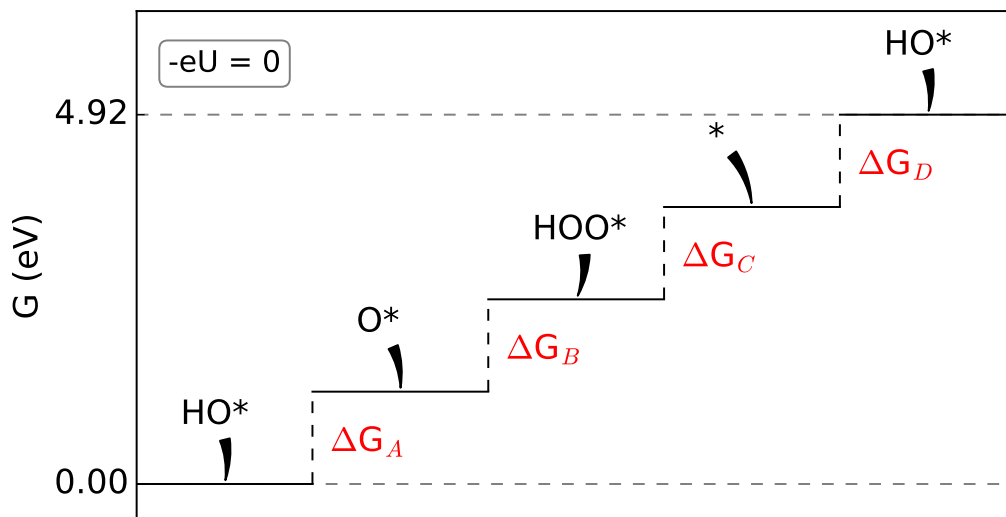


Figure 3.3: A schematic energy landscape with the intermediate surface species marked out on each step. The red free energies are the reaction free energies in eq 3.13a-3.13d.

4

Results

The results are presented in this chapter along with a discussion. Section 4.1 details the bulk calculations including convergence tests of parameters as well as material characterization, which were performed to find an accurate computational setup. The results from the characterization study also serve as a validation of the calculations when the values are compared to those previously reported in the literature.

In section 4.2 the surface properties, such as surface energy, artificial electric field and charge analysis is presented. The results in this section further establishes the accuracy of the calculation but also provide insight in the properties of the 3C-SiC(111) surface.

In section 4.3 the main results of the project is presented and discussed. The free energy landscape of the intermediate reactions as well as the effect of external and photo-induced potential bias are shown, giving an indication of the efficiency.

Finally, in section 4.4 the electronic configuration of both bulk and surface structure is presented and discussed.

4.1 Bulk properties

Initial convergence tests for the bulk structure is detailed in this section. Physical properties are also calculated and compared to reference values to confirm that the calculations yield accurate results.

4.1.1 Verifying convergence

Convergence tests with different energy cutoff and k -point meshes are presented in Figure 4.1 for bulk SiC, water molecule, oxygen molecule and atomic oxygen. The figures show the total energy for each system when the energy cutoff radius and k -point setup is varied and the parameters are considered to be converged when the energy difference is below 10 meV between each step.

The figures indicates that bulk crystal have slowest convergence for both parameters, giving converged cutoff energy and k -points of 500 eV and 3 k -points in each direction. The energy difference with varied k -points is negligible already from the gamma point for H₂O, O₂ and atomic oxygen but varies much more for the bulk. This is due to the dispersion of energy bands in SiC, meaning that the band energy varies with the k -points in the Brillouin zone. The molecules and the atom were put in a vacuum box with a 10 Å distance to the edges of the box in order to remove any interaction between the periodic images of the systems. The cells in real space

4. Results

are larger for the molecules than the bulk unit cell (around 20 \AA compared to $\sim 4.3 \text{ \AA}$), resulting in a finer k -point sampling for the molecules compared to the crystal, owing to the inverse proportionality between distances in real space and k -space.

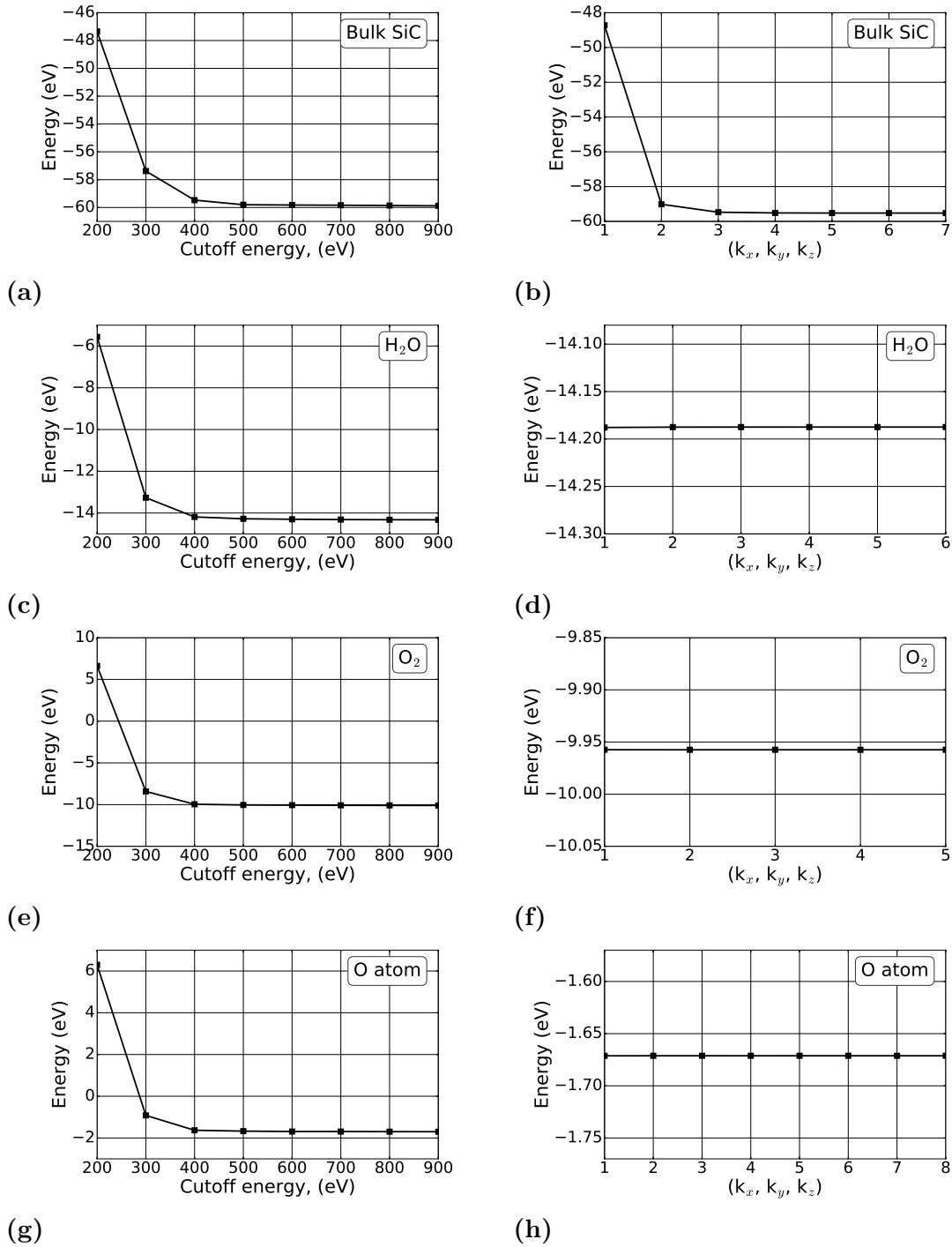


Figure 4.1: Convergence test on four different systems, bulk SiC, water molecule, oxygen molecule and atomic oxygen. The energy cutoff and number of k -points are varied and the total energy is calculated for each setup.

4.1.2 Bulk characterization

Since 3C-SiC has a cubic bulk unit cell the lattice parameter is determined by taking the cube root of its equilibrium volume (obtained from Figure A.1) by the method described in section 3.2.1. The obtained values are presented in Table 4.1 along with the calculated cohesive energy, energy of formation and bulk modulus. The values agree well with reference values, in particular the cohesive energy but also the lattice parameters. Notice, however, how the PBE and LDA functionals over- and underestimates the lattice parameter, respectively, compared to the experimental value. This is an expected outcome and it is known that these functionals usually exhibit this behaviour [36]. The calculated PBE lattice constant will be employed throughout the project. The characterization results strongly reassures that the calculations have a good accuracy.

Table 4.1: Calculated bulk quantities where a_0 is the lattice parameter, E_{coh} is the cohesive energy per SiC pair, E_{form} is the energy of formation per SiC pair and B is the bulk modulus. ^aref. [49], ^bref. [50], ^cref. [51], ^dref. [52], ^eref. [53].

	a_0 (Å)		E_{coh} (eV/pair)	E_{form} (eV/pair)	B (GPa)	
	PBE	LDA			PBE	LDA
This work	4.390	4.339	12.64	0.49	210.18	229.256
Ref. calc.	4.385 ^a	4.335 ^a	12.80 ^b	0.58 ^c	228 ^d	-
Exp.	4.36 ^{a,b}		12.68 ^b	0.68 ^c	225 ^e	

4.2 Surface properties

The slab is analysed to complete the computational setup before modeling the energy landscapes. Various physical properties are also studied to gain insight into the mechanisms of water oxidation on the surface.

4.2.1 Dipole corrections

The ESP along the vertical direction of the supercell is presented in Figure 4.2 at different vacuum widths. The figures represents a 10 atom layer thick slab, located in the vertical center of the cell, with an oxygen atom adsorbed on the Si-side. Moreover, the left panels shows the ESP without dipole correction and the right panels with dipole correction. The figures clearly shows that there is an electric field along the vertical axis, which is evident from the gradient of the ESP in the vacuum region. The work function differs with about 1.7 eV between the different sides of the slab. The results presented in Figure 4.2 are for slabs with an unsaturated bottom surface. However, hydrogen passivation appears to have a significant effect on the ESP, which can be seen in Figure A.2 in the appendix. Hydrogen passivation give rise to a significantly stronger electric field in the vacuum region with a work function difference of about 5 eV between the slab surfaces.

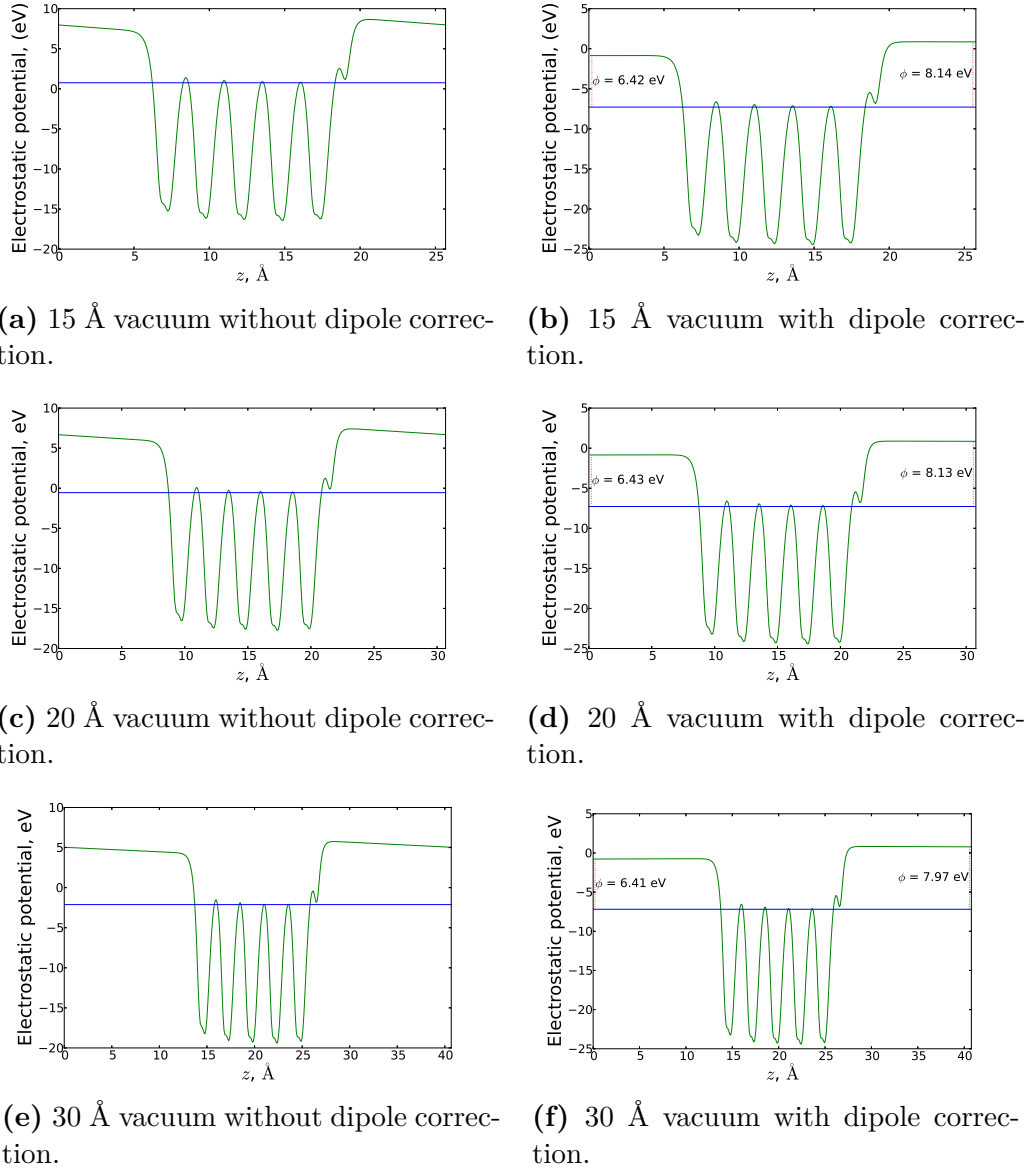


Figure 4.2: Electrostatic potential (green), at varied vacuum width, without dipole correction in the left panels and with dipole correction in the right panels. The blue line is the Fermi level and ϕ is the work function at the corresponding sides of the slab. The slab is oriented with the Si-side at high values of z and the C-side at low values.

4.2.2 Surface energies

Figure 4.3 shows that the surface energy appear to converge to 3000–3200 mJ/m² with varied parameter values, which is close to but somewhat higher than previously reported values [49]. The high energy indicate that the surface would prefer to reconstruct in order to lower the surface energy. The electrons of the surface atoms that are not involved in any bonds will be localized due to the semiconducting nature of 3C-SiC, which gives rise to dangling bonds at the surface. The number of dangling bonds can be lowered through surface reconstruction and thereby also the

surface energy. The structure optimization does however not result in any spontaneous reconstruction, implying that there is a tangible activation barrier between the phases.

The surface energy is also calculated as a means to measure convergence of the slab thickness, cutoff energy, vacuum width and k -point sampling. Figure 4.3 suggests that the convergence is reached for six atomic layers, energy cutoff of 500 eV and 6 Å vacuum width. The k -point sampling is shown with the number of k -points in the irreducible Brillouin zone in parentheses adjacent to the data points, which suggests that convergence is reached quite early.

A computational setup with an 8 layer thick slab, 4x4x1 k -point sampling and 600 eV energy cutoff is chosen based on these results. The cutoff is converged at 500 eV but a larger cutoff is chosen to have a margin of safety since a larger cutoff is not particularly computationally demanding.

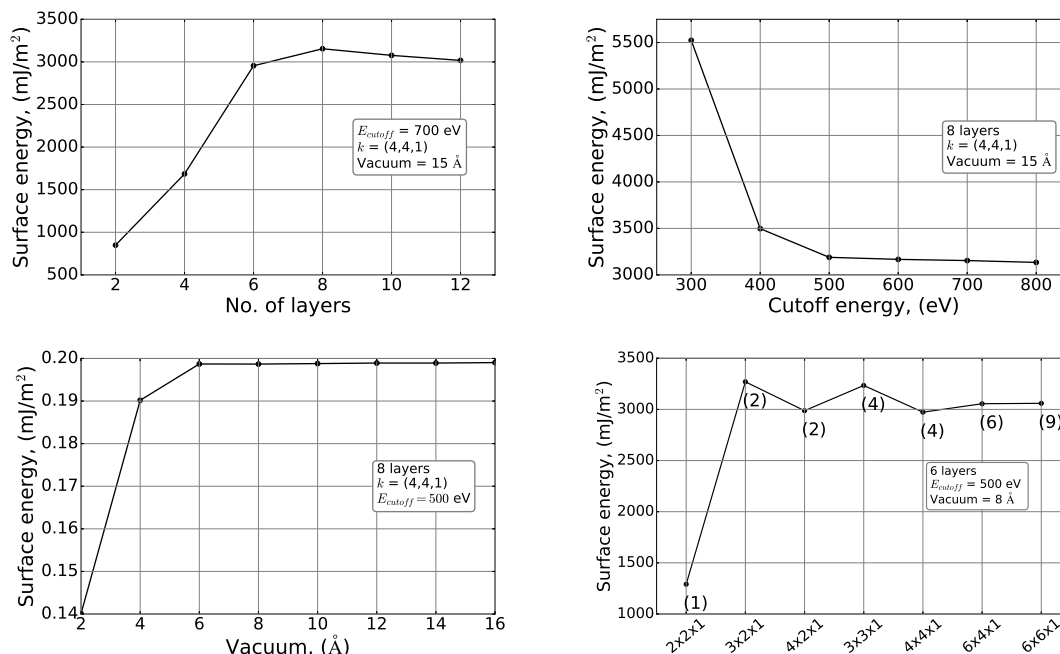


Figure 4.3: Surface energy of a bare slab with different thickness, energy cutoff, vacuum width and k -point sampling. The parentheses in the bottom right figure denote the number of k -points in the irreducible Brillouin zone.

The data in Figure 4.3 represent bare slabs but with adsorbates on the surface the induced dipole field could potentially yield slower convergence for the vacuum width due to interaction between the periodic mirror images. Therefore, in order to further ascertain convergence the adsorption energy of an oxygen atom on the Si side is calculated with varied vacuum width, which is presented in Figure 4.4. The figure does not show the actual adsorption energy of an oxygen atom but how the energy difference between a bare slab and a slab with an adatom varies with different vacuum.

Although the behaviour appears rather erratic the convergence is fairly distinguishable. The convergence is clearly slower compared to in Figure 4.3 where, for

comparison, the energy difference between 8 Å and 16 Å is 0.3 meV/Å². A large vacuum is however computationally expensive so it is set to 14 Å in all following calculations. This trade-off is considered acceptable since the energy discrepancies will not affect the results noticeably.

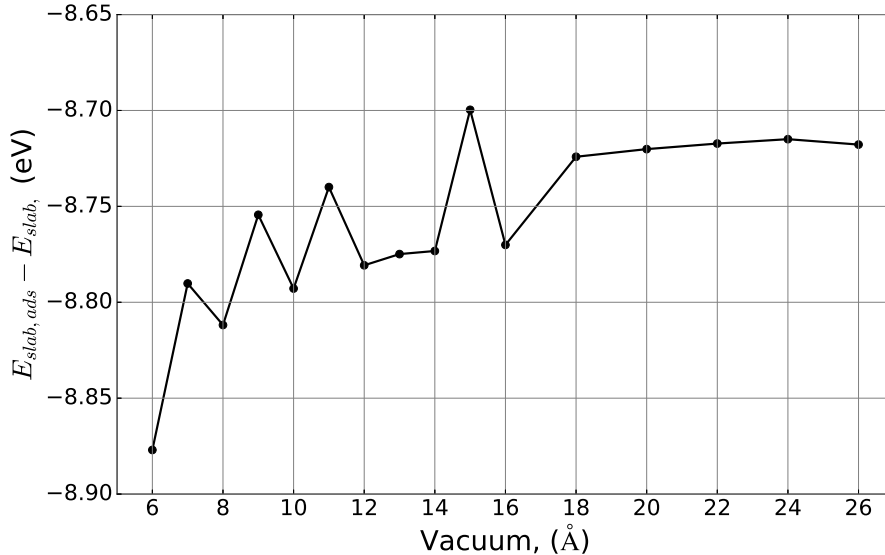


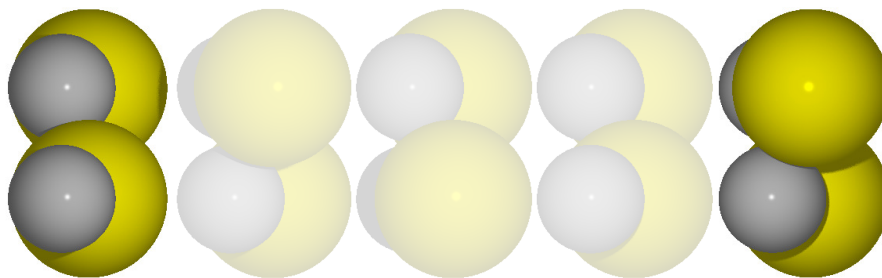
Figure 4.4: Energy difference between a slab with an oxygen adatom and a bare slab with different vacuum width.

4.2.3 Bader analysis

The electron density was found to be shifted from Si atoms towards C atoms, which was expected due to their difference in electronegativity. The charge analysis is performed on a 5 bilayer thick slab as well as an infinite bulk with the results presented in Table 4.2. The figure below helps clarifying which atoms in the the slab the tabulated data refers to. Bulk SiC appears to have a rather large charge transfer from Si atoms to the C atoms, which prevails in the surface. The surface atoms only bind to three atoms while the atoms below the surface bind to four atoms which explains the lower charge transfer at the surface. The charge transfer helps explaining the induced dipole field between the periodic slabs. The slab is asymmetric with one side being C-terminated and the other Si-terminated resulting in the electrostatic potential.

Table 4.2: The average charge transfer of the atomic species is presented for the surface atoms, subsurface and an infinite bulk.

	Surface	Subsurface	Bulk
q_C (C)	-2.189	-2.580	-2.698
q_{Si} (C)	2.011	2.674	2.698



4.3 Reaction energy landscape

The energy landscape is calculated for slabs having either bare or hydrogen passivated bottom surface. Both slabs are studied with 1/2 ML coverage of adsorbates on the Si-side where all adsorbates are in an ontop site. The slab without hydrogen passivation is furthermore also studied with full coverage where half of the adsorbates are hydroxyl molecules which does not participate in the reaction. Hydroxyl molecules are chosen since water is believed to dissociate into hydrogen atoms and hydroxyl groups on the bare surface.

The energy landscape for the slab without hydrogen passivation is shown in Figure 4.5 and the slab with passivation in Figure 4.6. The figures show the three cases where no bias is applied, only bias corresponding to solar illumination is applied and when enough bias is applied to overcome the overpotential.

In all calculations an external bias is needed, in addition to the photo-induced potential, to drive the reaction, implying that 3C-SiC is not feasible as photoanode in a self-sustained PEC. The additional potential needed for the slabs without hydrogen passivation are 1.45 eV for the 1/2 ML slab and 0.47 eV for the 1 ML slab and 1.05 eV for the hydrogen passivated slab. In all cases the overpotential occurs in the formation of a free surface site. This is reasonable given the relatively high surface energy for bare 3C-SiC, which implies that it likes to be covered by adatoms. A slight uphill step can also be seen in the first reaction step in Figure 4.5b when only light is applied. In this case the surface is initially covered of a full layer of hydroxyl groups so the increase in reaction energy is likely owing to the breaking of hydrogen bonds between the hydroxyl groups.

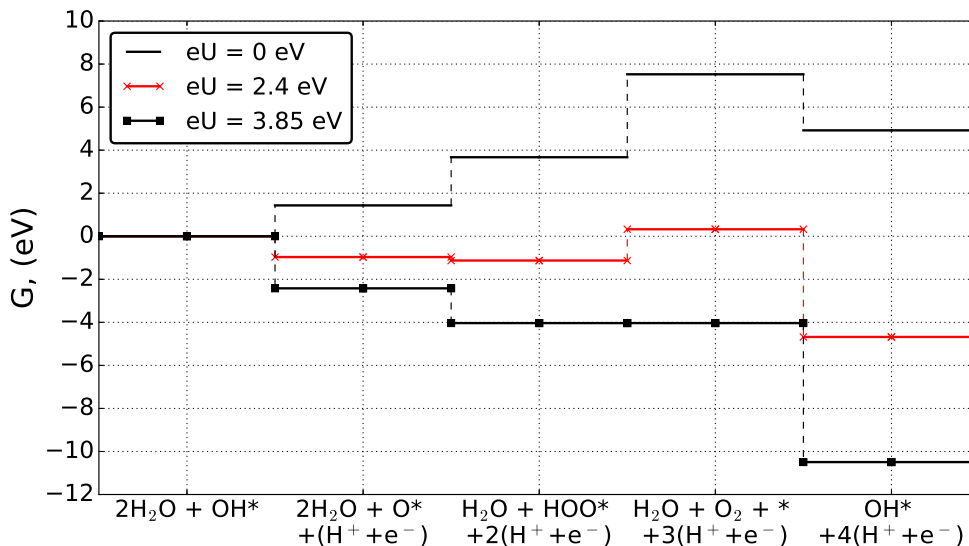
Further studies must however be made in order to determine to a certain degree whether self-sustained water oxidation is possible or not. The two major obstacles for the reaction according to the energy landscapes are the energy needed to form a free surface site and breaking the hydrogen bonds on the fully hydroxyl covered surface. It is possible that a reconstructed surface would form free sites easier, thus

Table 4.3: Entropic and zero-point energy contributions in eV.

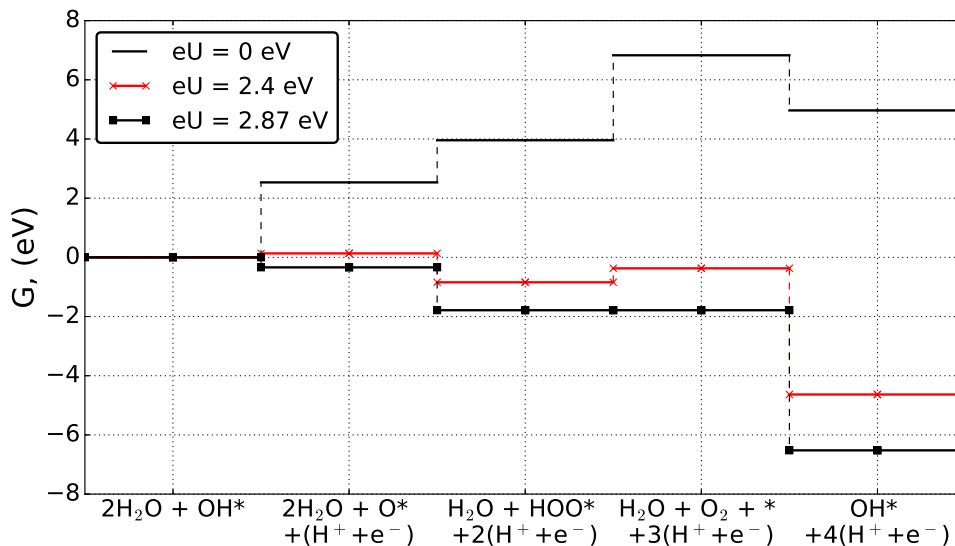
	TS (298 K)	ZPE
H ₂ O	0.671 (35 mbar)	0.584
O ₂	0.635	0.137
H ₂	0.403	0.280
H ⁺	0.201	0.069
O*	0.063	0.073
OH*	0.072	0.398
OOH*	0.034	0.458

4. Results

reducing the reaction energy, if the surface energy of the bare slab is lower than it is for the (1×1) phase studied here. Furthermore, with larger lateral unit cells the number of inert hydroxyl groups per reacting hydroxyl groups could increase for the 1 ML coverage. This would reduce the number of broken hydrogen bonds and likely the energy required to deprotonate one of the hydroxyl groups.



(a) 1/2 ML hydroxyl coverage without hydrogen passivation.



(b) 1 ML hydroxyl coverage without hydrogen passivation.

Figure 4.5: The figures show the energy landscape for a slab without hydrogen passivated bottom surface. The lines represents dark condition (0 eV), illuminated condition (2.4 eV) and the potential needed to overcome the overpotential (>2.4 eV).

The entropies and zero-point corrections are presented in Table 4.3. The values for the proton are just taken to be half of the corresponding hydrogen molecule

values. The entropy is clearly much smaller for the adsorbed species than for the molecules in the gas-phase. The entropy is calculated at 298 K for all species and atmospheric pressure for all molecules apart from water which is calculated at 35 mbar as discussed in section 3.5.1. The obtained values agree well with previously reported values [41].

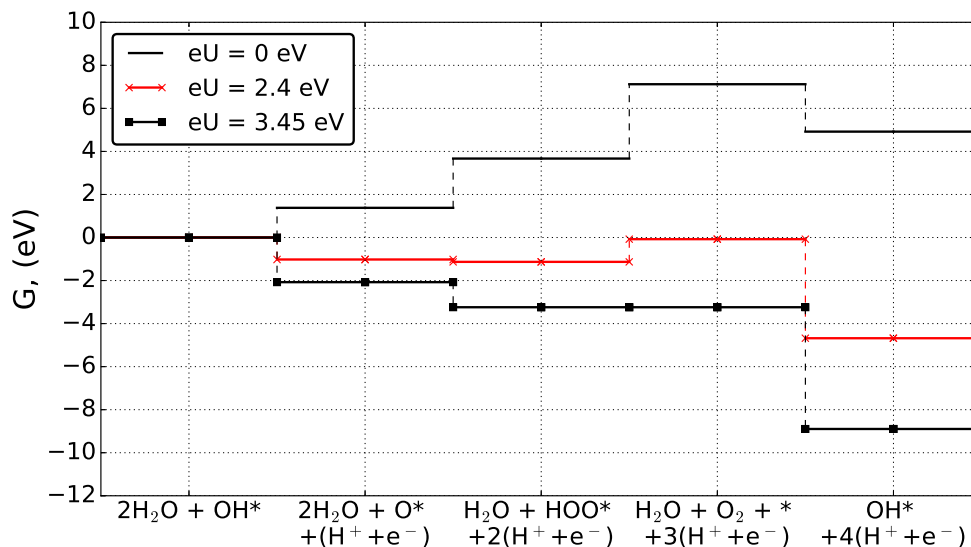


Figure 4.6: Energy landscape with 1/2 ML hydroxyl coverage and hydrogen passivated bottom surface.

4.4 Electronic configuration

The electronic structure is studied for the bulk and slab to further understand properties relevant for mechanisms involved in water oxidation. The density of states is primarily studied but also the band structure for the bulk. Additional information can be found in section A.4 in the appendix.

4.4.1 Bulk

The band structure and DOS for the bulk is presented in Figure 4.7. As is expected in DFT the band gap is underestimated to 1.80 eV compared to experimental values of 2.4 eV [10]. Both the band structure and DOS however agree well with previous local DFT calculations [54,55]. Moreover, the band structure shows that 3C-SiC exhibits an indirect band gap between the Γ and X point which lowers the probability for the material to absorb photons of band gap energies. Apart from absorbing the photon energy the electron also need to change its momentum by coupling with a phonon in order to make the band transition. The indirect band gap does however similarly lower the probability of electron-hole recombination and thus increase the charge carrier lifetime.

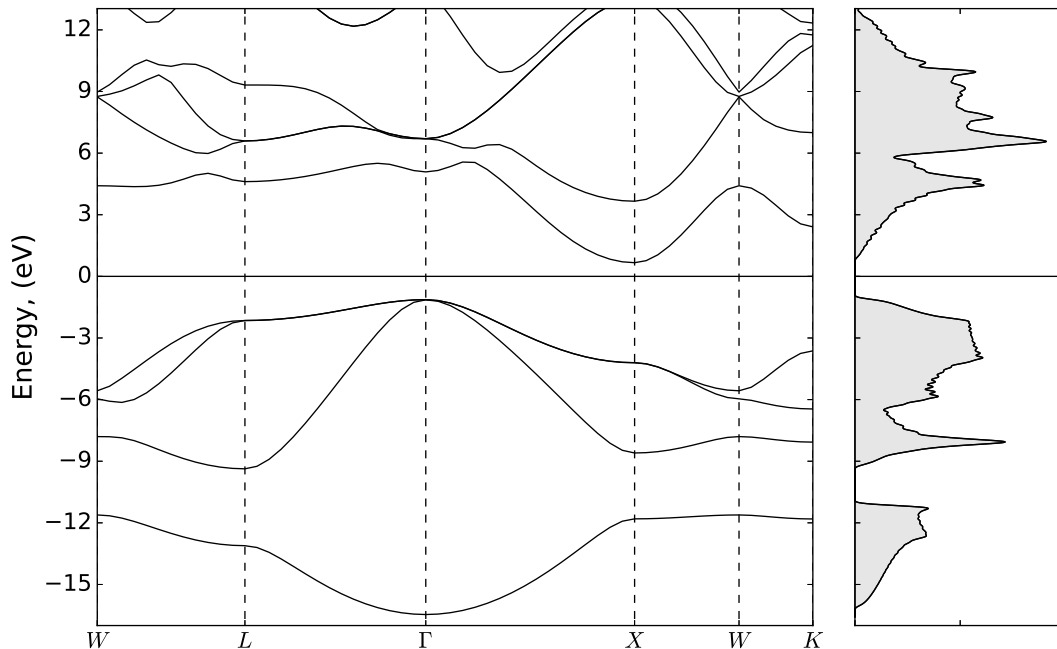


Figure 4.7: Band structure and DOS for bulk 3C-SiC. The indirect band gap is visible in the band structure.

4.4.2 Slab

The density of states for the slab is presented for a slab without passivated bottom surface in Figure 4.8 and for a hydrogen passivated slab in Figure 4.9. Each slab is studied in the three cases where the Si-side is either entirely free from adsorbate, covered by 1/2 ML hydroxyl groups or 1 ML of hydroxyl groups. The most prominent feature compared to the bulk DOS is the spike in the band gap, which is caused by the unsaturated surface sites. The metallic state in the band gap vanishes completely for the hydrogen passivated slab with 1 ML coverage but not for the slab without bottom passivation full hydroxyl coverage. This indicates that the states are primarily caused by the unsaturated C-atoms at the bottom. This is further supported in Figure A.5 where the wavefunctions are plotted. Appendix A.4 also includes narrower plots of Figures A.3 and A.4 around the band gap where the effect of bond saturation becomes more clear.

The metallic states for the slab could influence how the surface interacts with molecules at the surface. Depending on the position of the molecules bonding and antibonding orbitals the metallic state and Fermi level the surface could, for instance, weaken the intra-molecular bonds and cause it to dissociate and adsorb on the surface. Other events are also possible where the metallic states prevent the molecule to adsorb on the surface. The influence of the metallic state on the interaction between the surface and water molecules are of particular interest for this study but will not be further investigated here.

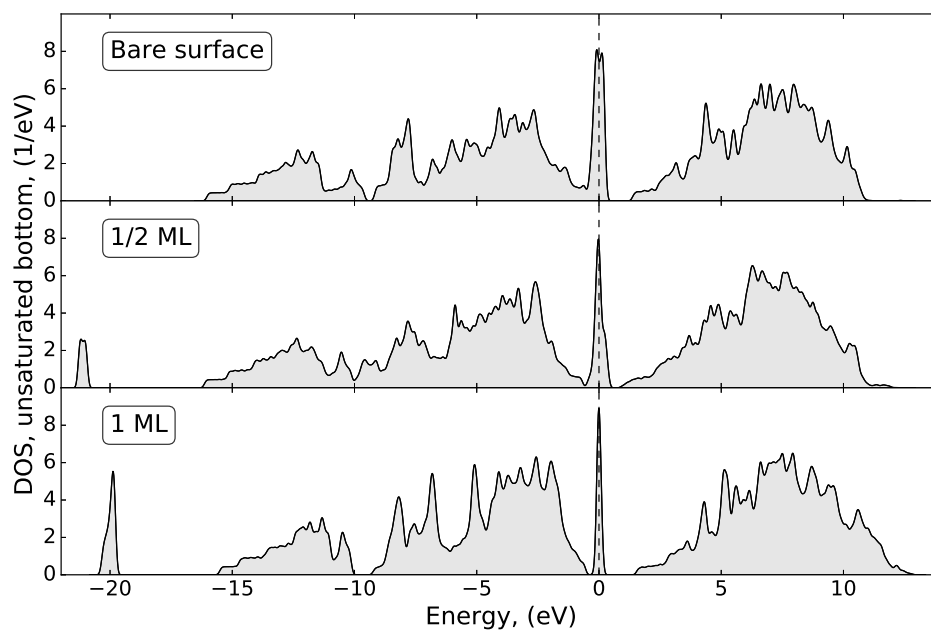


Figure 4.8: Density of states with different hydroxyl group coverage and without hydrogen passivation.

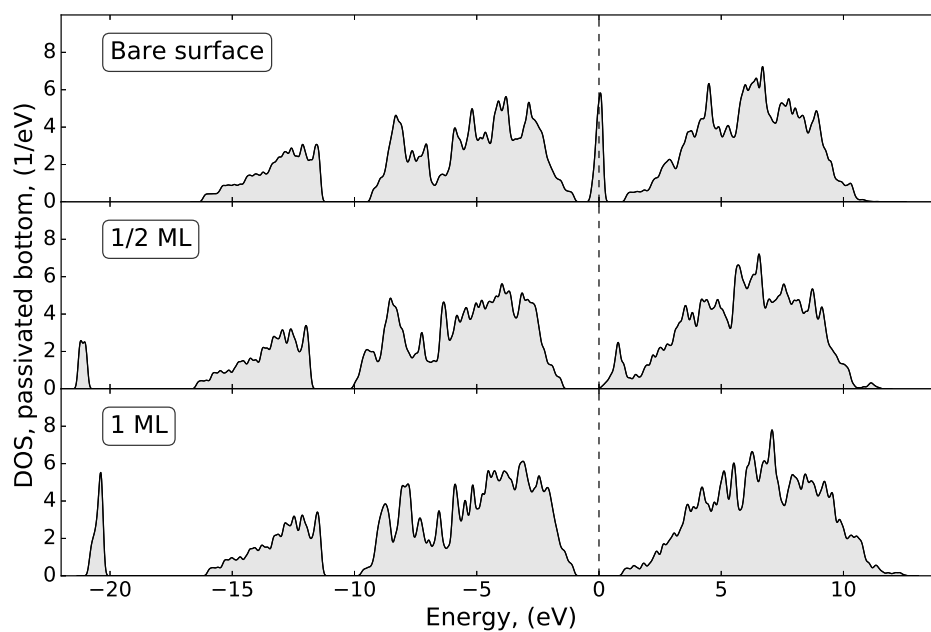


Figure 4.9: Density of states with different hydroxyl group coverage and with hydrogen passivation.

5

Conclusion

The photo-oxidation of water on the 3C-SiC(111)-(1×1) surface was studied, using first-principles calculations, where a four-step water oxidation pathway previously studied for several metal oxides was analysed. This cleaving of cubic SiC crystal has alternating Si and C atomic planes in the vertical direction resulting in an asymmetric slab, thus, having one Si-terminated surface and the other being C-terminated. The water oxidation reaction is in this project studied over the Si-terminated surface.

Convergence tests were carried out, first on bulk structure and then on slab structure, to find a suitable computational model. The cutoff energy and k -point mesh were converged with respect to the total energy of the bulk unit cell. Similarly, the cutoff energy, k -point mesh, vacuum width and number of atomic layers were converged for the slab with respect to the surface energy. Physical properties, such as bulk modulus and formation energy for the bulk, were also calculated and compared with reference values from the literature to verify the accuracy of the calculations.

All calculations indicate that a photo-induced potential only is not sufficient to drive the reaction but an external potential, of at least 0.47 V, is required as well, thus implying that 3C-SiC(111) is not appropriate as a photoanode. The results are however not conclusive and further studies must be done to gain full understanding of its water-splitting capabilities. The major contribution to the overpotential is the high surface energy of the clean surface which makes desorption of HOO* very energy demanding. A reconstructed surface would likely have lower surface energy and could therefore be favourable for water oxidation. The calculations also show that the overpotential is lowered with about 1 V if all free sites are covered by hydroxyl groups. This, however, creates a network of hydrogen bonds, which makes the deprotonation of OH* into O* more difficult. This effect can potentially be mitigated by increasing the lateral size of the unit cell. As a high coverage of hydroxyl groups is likely from dissociation of water on the surface a larger lateral unit cell could reduce the energy needed to deprotonate a few of these hydroxyl groups.

An important remark is also that kinetic overpotentials are not accounted for in these calculations. The activation barrier in the reaction coordinate can not be overlooked for a complete understanding of the water oxidation. This is however beyond the scope of this study and instead a subject of future studies.

Bibliography

- [1] "Paris Agreement, FCCC/CP/2015/L.9/Rev.1". UNFCCC secretariat. Retrieved 11 September 2016.
URL: <http://unfccc.int/resource/docs/2015/cop21/eng/l09r01.pdf>
- [2] IPCC, 2014: Climate Change 2014: Mitigation of Climate Change. Contribution of Working Group III to the Fifth Assessment Report of the Intergovernmental Panel on Climate Change [Edenhofer, O., R. Pichs-Madruga, Y. Sokona, E. Farahani, S. Kadner, K. Seyboth, A. Adler, I. Baum, S. Brunner, P. Eickemeier, B. Kriemann, J. Savolainen, S. Schlömer, C. von Stechow, T. Zwickel and J.C. Minx (eds.)]. Cambridge University Press, Cambridge, United Kingdom and New York, NY, USA.
- [3] Grätzel M. *Nature*. **2001**, 414, 338.
- [4] Lewis N S, Nocera D G. *PNAS*. **2006**, 103(43), 15729.
- [5] Valdés Á, Brillet J, Grätzel M, Gudmundsdóttir H, Hansen H A, Jónsson H et al. *Phys. Chem. Chem. Phys.* **2012**, 14, 49.
- [6] Fujishima A, Honda K. *Nature*. **1972**, 238, 37.
- [7] Kato M, Yasuda T, Miyake K, Ichimura M. *Int. J. Hydrogen Energy*. **2014**, 39, 4845.
- [8] Yasuda T, Kato M, Ichimura M, Hatayama T. *Appl. Phys. Lett.* **2012**, 101, 053902.
- [9] Walter M G, Warren E L, McKone J R, Boettcher S W, Mi Q, Santori E A, Lewis N S. *Chem. Rev.* **2010**, 110(11), 6446.
- [10] Ma Q-B, Ziegler J, Kaiser B, Fertig D, Calvet W, Murugasen E, Jaegermann W. *Int. J. Hydrogen Energy*. **2014**, 39, 1623.
- [11] The data is taken from the Thomson Reuters search engine Web Of Science with search keywords "*SiC*", "*water-splitting*" and "*photo**" in either the title or abstract.
- [12] Yasuda T, Kato M, Ichimura M, Hatayama T. *Mater. Sci. Forum*. **2013**, 740-742, 859.
- [13] Ma Q-B, Kaiser B, Ziegler J, Fertig D, Jaegermann W. *J. Phys. D: Appl. Phys.* **2012**, 45, 325101.
- [14] Cicero G, Galli G, Catellani A. *J. Phys. Chem. B*. **2004**, 108, 16518.

- [15] Catellani A, Cicero G, Righi M C, Pignedoli C A. *Mater. Sci. Forum.* **2005**, 483-485, 541.
- [16] Amy F, Chabal Y J. *J. Chem. Phys.*, **2003**, 119, 6201.
- [17] Amy F. *J. Phys. D: Appl. Phys*, **2007**, 40, 6201.
- [18] Du J, Wen B, Melnik R. *Comput. Mater. Sci.*, **2014**, 95, 451.
- [19] Kaplan R. *Surface Science.* **1989**, 215, 111.
- [20] Starke U, Schardt J, Bernhardt J, Franke M, Reuter K, Wedler H et al. *Phys. Rev. Lett.* **1998**, 80(4), 758.
- [21] Luo X, Qian G, Fei W, Wang E G, Chen C. *Phys. Rev. B.* **1998**, 57(15), 9234.
- [22] Atkins P, Jones L. *Chemical principles: The quest for insight*. 5th ed. New York: W. H. Freeman and Company; 2010.
- [23] Sze S M, Kwok K Ng. *Physics of Semiconductor Devices*. 3rd ed. John Wiley & Sons, Inc; 2006.
- [24] Memming R. *Electrochimica Acta.* **1980**, 25, 77.
- [25] Nozik A J, Memming R. *J. Phys. Chem.* **1996**, 100, 13061.
- [26] Bozak M J. *Phys. Stat. Sol. (b)*. **1997**, 202, 549.
- [27] Dau H, Limberg C, Reier T, Risch M, Roggan S, Strasser P. *ChemCatChem.* **2010**, 2, 724.
- [28] Perdew J P, Burke K, Ernzerhof Z. *Phys. Rev. Lett.*, **1996**, 77, 3865.
- [29] Born M, Oppenheimer J R. *Ann. Physik*, **1927**, 84, 457.
- [30] Hohenberg P, Kohn W. *Phys. Rev.*, **1964**, 136, B864.
- [31] Kohn W, Sham L J. *Phys. Rev.*, **1965**, 140, A1133.
- [32] Martin R M. *Electronic structure: basic theory and practical methods*. Cambridge University Press; 2004.
- [33] "Annual DFT Popularity Poll 2015". Swart M, Bickelhaupt F M, Duran M. URL: <http://www.marcelswart.eu/>
- [34] Blöchl P E. *Phys. Rev. B*, **1994**, 50, 17953.
- [35] Monkhorst H J, Pack J D. *Phys. Rev. B*, **1976**, 13, 5188.
- [36] Haas P, Tran F, Blaha P. *Phys. Rev. B*, **2009**, 79 085104.
- [37] Neugebauer J, Scheffler M. *Phys. Rev. B*, **1992**, 46(24), 16067.
- [38] Bengtsson L. *Phys. Rev. B*, **1998**, 59, 12301.
- [39] Bader R F W. *Atoms in Molecules: A Quantum Theory*. **1990**; New York, Oxford University Press.
- [40] Henkelman G, Arnaldsson A, Jónsson H. *Comput. Mater. Sci.* **2006**, 26, 354.
- [41] Valdés Á, Qu Z-W, Kroes G-J, Rossmeis J, Nørskov J K. *J. Phys. Chem. C*, **2008**, 112, 9872.
- [42] Valdés Á, Kroes G-J. *J. chem. Phys*, **2009**, 130, 114701.

-
- [43] Friebel D et al. *J. Chem. Phys.*, **2015**, 137, 1305.
- [44] Hellman A, Pala R G S. *J. Phys. Chem. C*, **2011**, 115, 12901.
- [45] Montoya J H, Garcia-Mota M, Nørskov J K, Vojodic A. *Phys. Chem. Chem. Phys.*, **2015**, 17, 2634.
- [46] Nørskov J K, Rossmeisl J, Logadottir A, Lindqvist L, Kitchin J R, Bligaard T, Jónsson H. *J. Phys. Chem. B*, **2004**, 108, 17886.
- [47] Chorkendorff I, Niemantsverdriet J W, Concepts of Modern Catalysis and Kinetics. 2nd ed. Weinheim: Wiley-VCH; 2007.
- [48] Cramer C J. Essentials of Computational Chemistry: Theories and Models. 2nd ed. West Sussex: Wiley; 2004.
- [49] Wang J, Zhang L, Zeng Q, Vignoles G L, Cheng L, Guette A. *Phys. Rev. B*, **2009**, 79, 125304
- [50] Jiang M, Peng S M, Zhang H B, Xu C H, Xiao H Y, Zhao F A, Liu Z J, Zu X T. *Scientific Reports*, **2016**, 6, 20669.
- [51] Abavare E K K, Iwata J-I, Yaya A, Oshiyama A. *Phys. Status Solidi B*, **2014**, 251, 1408.
- [52] Iuga M, Steinle-Neumann G, Meinhardt J. *Eur. Phys. J. B*, **2007**, 58, 127.
- [53] Lambrecht W R L, Segall B, Methfessel M, Schilfgaard M. *Phys. Rev. B*, **1991**, 44, 3685.
- [54] Zhao G L, Bagayoko D. *New Journal of Physics*. **2000**, 2, 16.1.
- [55] Ching W Y, Xu Y-N, Rulis P, O L. *Materials Science and Engineering A*. **2005**, 422, 147.

A

Appendix

A.1 Full free energy expressions

$$\Delta G_A = \Delta E_A + \frac{1}{2}E_{H_2} + (\Delta ZPE - T\Delta S)_A - eU \quad (\text{A.1a})$$

$$\Delta E_A = E_{O^*} - E_{HO^*}$$

$$(\Delta ZPE - T\Delta S)_A = (ZPE - TS)_{\{O^* + \frac{1}{2}H_2 - HO^*\}}$$

$$\Delta G_B = \Delta E_B + \frac{1}{2}E_{H_2} - E_{H_2O} + (\Delta ZPE - T\Delta S)_B - eU \quad (\text{A.1b})$$

$$\Delta E_B = E_{HOO^*} - E_{O^*}$$

$$(\Delta ZPE - T\Delta S)_B = (ZPE - TS)_{\{HOO^* + \frac{1}{2}H_2 - O^* - H_2O\}}$$

$$\Delta G_C = 4.92 + \Delta E_C + 2E_{H_2O} - \frac{3}{2}E_{H_2} + (\Delta ZPE - T\Delta S)_C - eU \quad (\text{A.1c})$$

$$\Delta E_C = E_* - E_{HOO^*}$$

$$(\Delta ZPE - T\Delta S)_C = (ZPE - TS)_{\{2H_2O - \frac{3}{2}H_2 - HOO^*\}}$$

$$\Delta G_D = \Delta E_D + \frac{1}{2}E_{H_2} - E_{H_2O} + (\Delta ZPE - T\Delta S)_D - eU \quad (\text{A.1d})$$

$$\Delta E_D = E_{HO^*} - E_*$$

$$(\Delta ZPE - T\Delta S)_D = (ZPE - TS)_{\{HO^* + \frac{1}{2}H_2 - H_2O\}}$$

The oxygen molecule is treated by considering the total water-splitting reaction, where the free energy is determined experimentally.



This can be expressed as

$$4.92 = G_{\text{O}_2} + 2G_{\text{H}_2} - 2G_{\text{H}_2\text{O}} \implies G_{\text{O}_2} = 4.92 + 2G_{\text{H}_2\text{O}} - 2G_{\text{H}_2} \quad (\text{A.2})$$

which, inserted in ΔG_C , gives

$$\begin{aligned} \Delta G_C &= \Delta E_C + G_{\text{O}_2} + \frac{1}{2}G_{\text{H}_2} = 4.92 + \Delta E_C + 2G_{\text{H}_2\text{O}} - 2G_{\text{H}_2} + \frac{1}{2}G_{\text{H}_2} = \\ &= 4.92 + \Delta E_C + 2G_{\text{H}_2\text{O}} - \frac{3}{2}G_{\text{H}_2} \end{aligned} \quad (\text{A.3a})$$

A.2 Lattice parameter

In order to determine the equilibrium lattice parameter the size of the unit cell is varied and the energy is calculated for each variation. Since the unit cell is cubic the lattice parameter is given by the cube root of the volume in Figure A.1 corresponding to the minimum in energy.

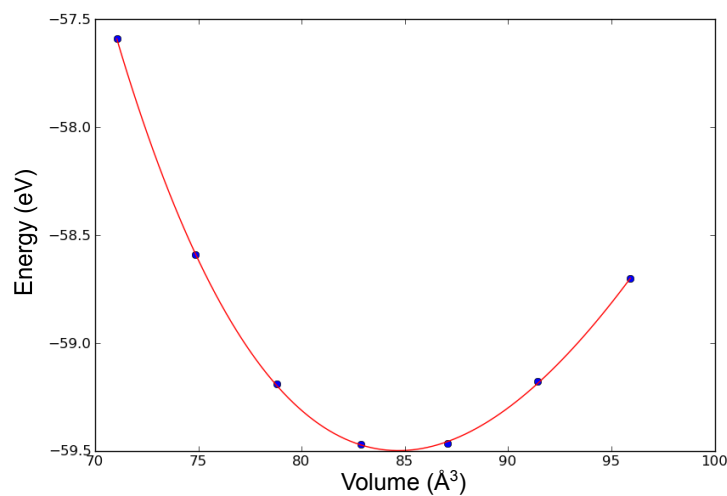
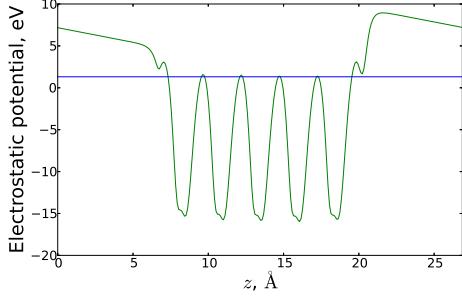
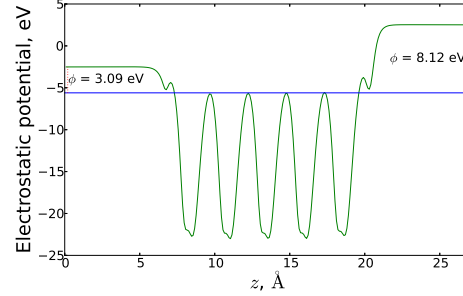


Figure A.1: Energy with varied cell volume. The lattice parameter is determined from the critical point.

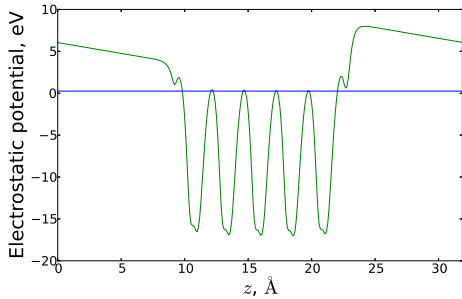
A.3 Dipole correction with hydrogen passivation



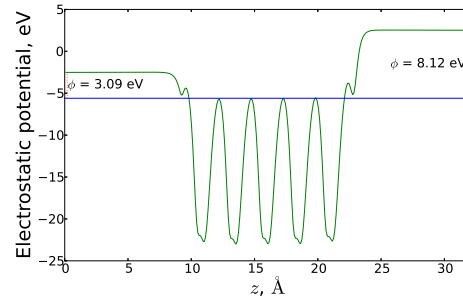
(a) Hydrogen passivated slab in 15 Å vacuum without dipole correction.



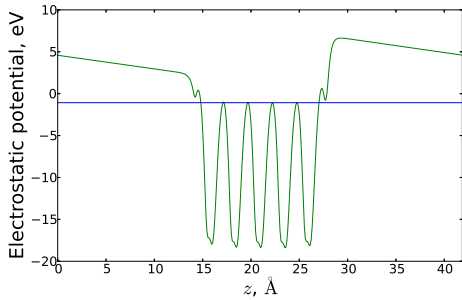
(b) Hydrogen passivated slab in 15 Å vacuum with dipole correction.



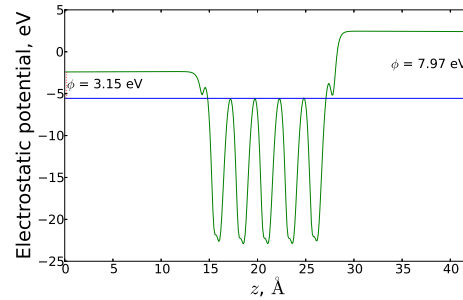
(c) Hydrogen passivated slab in 20 Å vacuum without dipole correction.



(d) Hydrogen passivated slab in 20 Å vacuum with dipole correction.



(e) Hydrogen passivated slab in 30 Å vacuum without dipole correction.



(f) Hydrogen passivated slab in 30 Å vacuum with dipole correction.

Figure A.2: Electrostatic potential (green), at varied vacuum width, without dipole correction in the left panels and with dipole correction in the right panels. The blue line is the fermi level and ϕ is the work function at the corresponding sides of the slab. The slab is oriented with the Si-side at high values of z and the C-side at low values.

A.4 Electronic structure

Figure A.3 and A.4 shows the DOS in the band gap region for a slab without hydrogen passivation and with hydrogen passivation respectively (compare with Figure 4.8 and 4.9).

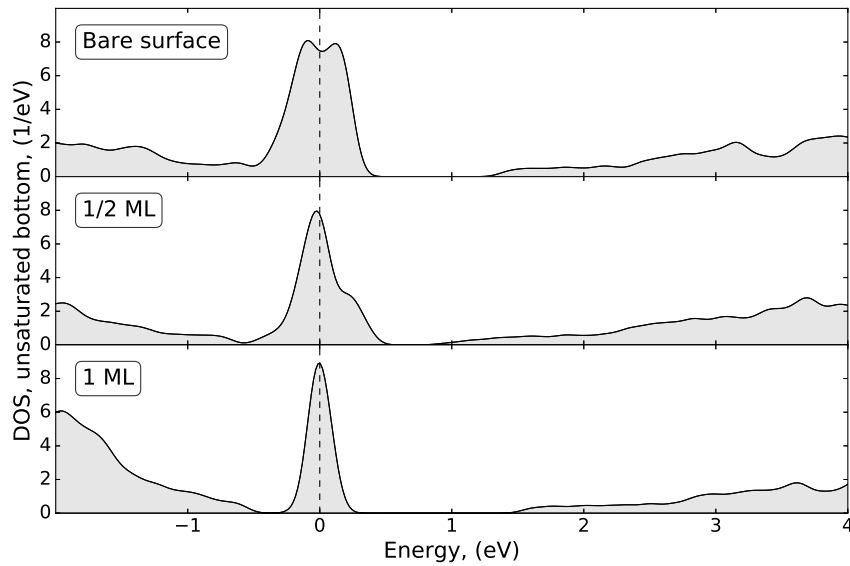


Figure A.3: Density of states for a four atomic layer thick slab without hydrogen passivation.

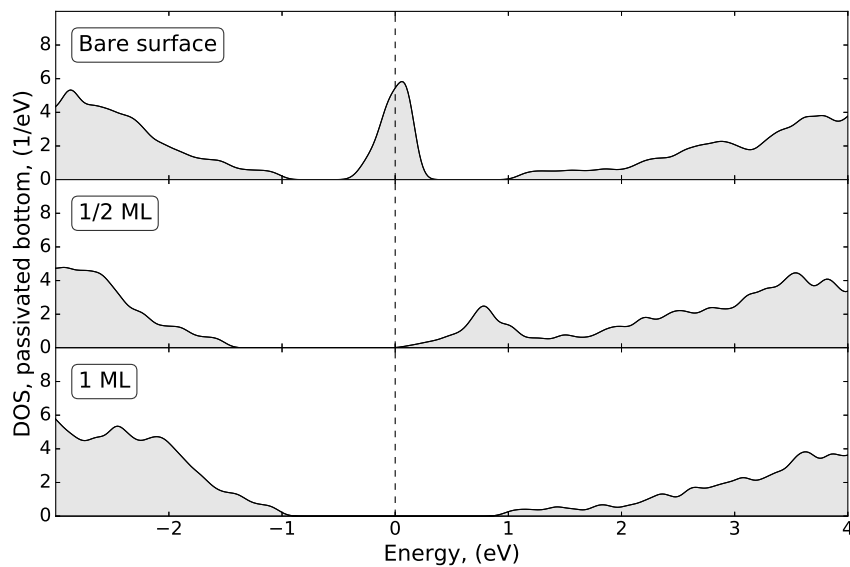


Figure A.4: Density of states for an eight atomic layer thick slab with hydrogen passivation.

The wavefunctions close to the Fermi level in the valence band is shown in Figure A.5 for the slab. The isosurface level is $0.10 \text{ \AA}^{-3/2}$, meaning that the isosurfaces contains all data points larger than that and excludes all lower values. The maximum values of the wavefunctions for the slab without and with hydrogen passivation respectively is $0.53 \text{ \AA}^{-3/2}$ and $0.41 \text{ \AA}^{-3/2}$.

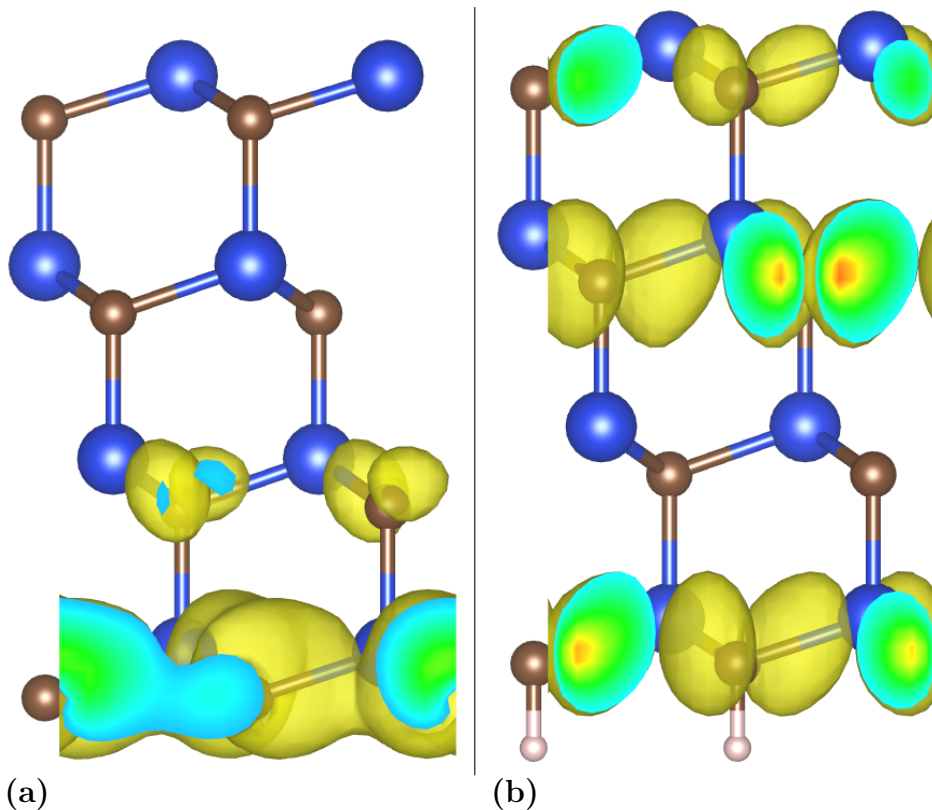


Figure A.5: Wavefunctions at Fermi level without hydrogen passivation (left) and with hydrogen passivation (right).

A.5 Free energies

The following tables contains the raw data to the energy landscape Figures 4.5 and 4.6 in the results.

Table A.1: Reaction free energy for 1/2 ML coverage without hydrogen passivation, corresponding to Figure 4.5a.

$-eU$ (eV)	ΔG_A (eV)	ΔG_B (eV)	ΔG_C (eV)	ΔG_D (eV)
0	1.43	2.24	3.85	-2.60
2.4	-0.97	-0.16	1.45	-5.00
3.85	-2.42	-1.62	0	-6.46

Table A.2: Reaction free energy for 1 ML coverage without hydrogen passivation, corresponding to Figure 4.5b.

$-eU$ (eV)	ΔG_A (eV)	ΔG_B (eV)	ΔG_C (eV)	ΔG_D (eV)
0	2.53	1.42	2.87	-1.86
2.4	0.13	-0.98	0.47	-4.26
2.87	-0.34	-1.45	0	-4.74

Table A.3: Reaction free energy for 1/2 ML coverage with hydrogen passivation, corresponding to Figure 4.6.

$-eU$ (eV)	ΔG_A (eV)	ΔG_B (eV)	ΔG_C (eV)	ΔG_D (eV)
0	1.38	2.29	3.45	-2.20
2.4	-1.02	-0.11	1.05	-4.60
3.45	-2.08	-1.16	0	-5.66